



# In-Situ Solid-Propellant Burn-Rate Measurements Using Flash Cineradiography

R. Y. Walker and R. A. Gamble  
Sverdrup Technology, Inc.  
and  
L. M. Smith  
University of Tennessee Space Institute

April 1986      PROPERTY OF UNITED STATES AIR FORCE  
AEDC TECHNICAL LIBRARY

Final Report for Period October 1, 1983 to September 30, 1984

**TECHNICAL REPORTS  
FILE COPY**

Approved for public release; distribution unlimited.

**ARNOLD ENGINEERING DEVELOPMENT CENTER  
ARNOLD AIR FORCE STATION, TENNESSEE  
AIR FORCE SYSTEMS COMMAND  
UNITED STATES AIR FORCE**

## NOTICES

When U. S. Government drawings, specifications, or other data are used for any purpose other than a definitely related Government procurement operation, the Government thereby incurs no responsibility nor any obligation whatsoever, and the fact that the government may have formulated, furnished, or in any way supplied the said drawings, specifications, or other data, is not to be regarded by implication or otherwise, or in any manner licensing the holder or any other person or corporation, or conveying any rights or permission to manufacture, use, or sell any patented invention that may in any way be related thereto.

Qualified users may obtain copies of this report from the Defense Technical Information Center.

References to named commercial products in this report are not to be considered in any sense as an endorsement of the product by the United States Air Force or the Government.

This report has been reviewed by the Office of Public Affairs (PA) and is releasable to the National Technical Information Service (NTIS). At NTIS, it will be available to the general public, including foreign nations.

## APPROVAL STATEMENT

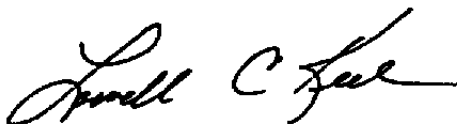
This report has been reviewed and approved.



DAVID A. DUESTERHAUS  
Directorate of Technology  
Deputy for Operations

Approved for publication:

FOR THE COMMANDER



LOWELL C. KEEL, Lt Colonel, USAF  
Director of Technology  
Deputy for Operations

UNCLASSIFIED

SECURITY CLASSIFICATION OF THIS PAGE

REPORT DOCUMENTATION PAGE				
1a REPORT SECURITY CLASSIFICATION <b>UNCLASSIFIED</b>		1b. RESTRICTIVE MARKINGS		
2a SECURITY CLASSIFICATION AUTHORITY		3. DISTRIBUTION/AVAILABILITY OF REPORT <b>SEE REVERSE OF THIS PAGE</b>		
2b DECLASSIFICATION/DOWNGRADING SCHEDULE				
4 PERFORMING ORGANIZATION REPORT NUMBER(S) <b>AEDC-TR-85-22</b>		5 MONITORING ORGANIZATION REPORT NUMBER(S)		
6a. NAME OF PERFORMING ORGANIZATION <b>Arnold Engineering Development Center</b>	6b. OFFICE SYMBOL <i>(If applicable)</i> <b>DOT</b>	7a. NAME OF MONITORING ORGANIZATION		
6c. ADDRESS <i>(City, State and ZIP Code)</i> <b>Air Force Systems Command Arnold Air Force Station, TN 37389-5000</b>		7b. ADDRESS <i>(City, State and ZIP Code)</i>		
8a. NAME OF FUNDING/SPONSORING ORGANIZATION <b>Arnold Engineering Development Center</b>	8b. OFFICE SYMBOL <i>(If applicable)</i> <b>DO</b>	9. PROCUREMENT INSTRUMENT IDENTIFICATION NUMBER		
8c. ADDRESS <i>(City, State and ZIP Code)</i> <b>Air Force Systems Command Arnold Air Force Station, TN 37389-5000</b>		10 SOURCE OF FUNDING NOS		
11 TITLE <i>(Include Security Classification)</i> <b>SEE REVERSE OF THIS PAGE</b>		PROGRAM ELEMENT NO <b>65807F</b>	PROJECT NO	TASK NO
		WORK UNIT NO.		
12 PERSONAL AUTHOR(S) <b>Walker, R. Y. and Gamble, R. A., Sverdrup Technology, Inc., AEDC Group and (Cont)</b>				
13a. TYPE OF REPORT <b>Final</b>	13b. TIME COVERED <b>FROM 10/1/83 TO 9/30/84</b>	14 DATE OF REPORT <i>(Yr, Mo, Day)</i> <b>April 1986</b>	15 PAGE COUNT <b>46</b>	
16. SUPPLEMENTARY NOTATION <b>Available in Defense Technical Information Center (DTIC).</b>				
17 COSATI CODES		18. SUBJECT TERMS <i>(Continue on reverse if necessary and identify by block number)</i>		
FIELD	GROUP	SUB GR.		
21	09	2	flash radiography erosive burning	
14	05		solid propellants burn-rate measurements	
19 ABSTRACT <i>(Continue on reverse if necessary and identify by block number)</i> <p>Flash radiography has been applied to the measurement of solid-propellant burn rates during a series of solid-propellant rocket motor tests at AEDC. This technique offers the advantage of realistic operating conditions and higher data rates than other measurement techniques. The propellant grains were cylindrically perforated and had action times ranging from 2.2 to 3 sec. Four of the six motors were designed to exhibit varying degrees of erosive burning. Chamber pressure and axial thrust were measured on each of the tests. Approximately 25 radiographs (at a rate of 6 per second) were recorded during the tests. These radiographs were subjected to three different methods of image processing. In addition to the quantitative data obtained, many interesting burn anomalies were revealed in the radiographs.</p>				
20 DISTRIBUTION/AVAILABILITY OF ABSTRACT <b>UNCLASSIFIED/UNLIMITED <input type="checkbox"/> SAME AS RPT. <input checked="" type="checkbox"/> DTIC USERS <input type="checkbox"/></b>		21 ABSTRACT SECURITY CLASSIFICATION <b>UNCLASSIFIED</b>		
22a. NAME OF RESPONSIBLE INDIVIDUAL <b>W. O. Cole</b>		22b TELEPHONE NUMBER <i>(Include Area Code)</i> <b>(615)454-7813</b>	22c OFFICE SYMBOL <b>DOS</b>	

UNCLASSIFIED

SECURITY CLASSIFICATION OF THIS PAGE

3. DISTRIBUTION/AVAILABILITY OF REPORT

Approved for public release; distribution unlimited.

11. TITLE

In-Situ Solid-Propellant Burn-Rate Measurements Using Flash Cineradiography

12. PERSONAL AUTHORS

Smith, L. M., University of Tennessee Space Institute

UNCLASSIFIED

SECURITY CLASSIFICATION OF THIS PAGE

## **PREFACE**

The work reported herein was conducted by the Arnold Engineering Development Center (AEDC), Air Force Systems Command (AFSC), at the request of Air Force Rocket Propulsion Laboratory (AFRPL). The results of the test were obtained by Sverdrup Technology, Inc., AEDC Group, operating contractor for the propulsion test facilities at AEDC, AFSC, Arnold Air Force Station, Tennessee under Project Number DA39EW. The Air Force Project Manager was David A. Duesterhaus, AF/DOTR. The Project Monitor at AFRPL was Lt. Col. Homer Pressley, Jr. The manuscript was submitted for publication on March 4, 1985.

## CONTENTS

	<u>Page</u>
1.0 INTRODUCTION .....	5
2.0 DISCUSSION OF SOLID-PROPELLANT COMBUSTION .....	6
2.1 Burn-Rate Measurements .....	6
2.2 Burn-Rate Characteristics .....	7
3.0 TEST DESCRIPTION .....	8
3.1 Test Article Description .....	8
3.2 Test Facility Description .....	9
3.3 X-Ray System Description .....	10
4.0 RADIOGRAPHIC DATA REDUCTION .....	10
4.1 AFRPL Data Reduction Method .....	11
4.2 UTSI Data Reduction Method .....	12
4.3 AEDC Data Reduction Method .....	13
5.0 RESULTS .....	15
5.1 Test Summary .....	15
5.2 Burn-Rate Data .....	15
5.3 Burn Anomalies .....	17
6.0 CONCLUSION .....	17
REFERENCES .....	18

## ILLUSTRATIONS

### Figure

1. Test Article Configuration .....	21
2. Test Installation .....	22
3. X-Ray Cineradiography System .....	23
4. System for Monitoring Pulser Output .....	24
5. Ray-Tracing Process to Compute Port Area .....	25
6. One-Dimensional Ideal Image for Cylinder .....	26
7. One-Dimensional Degraded Image for Cylinder .....	27
8. Density Distribution of a Hollow Cylinder and Gradient .....	28
9. Chamber Pressure and Axial-Thrust Time Histories .....	29
10. Case Strain and Film-Change Event .....	30
11. Burn-Rate Measurement, Motor No. 6 .....	31
12. Burn-Rate Measurement, Motor No. 2 .....	32
13. Burn-Rate Measurement, Motor No. 3 .....	33

<u>Figure</u>	<u>Page</u>
14. Burn-Rate Measurement, Motor No. 5 .....	34
15. Port Diameters at Time Two-Thirds Through Burn .....	35
16. Comparison of UTSI and AEDC Burn Rates at Center of Motor No. 5 .....	36
17. Predicted and Measured Pressures for High Erosive Motor .....	37
18. Predicted and Measured Pressures for Mild Erosive Motor .....	38
19. Predicted and Measured Pressures for Nonerosive Motor .....	39

### TABLES

1. Propellant Formulation .....	40
2. Motor Geometry Parameters Affecting Erosive Burning Severity .....	40
3. Specifications of Cineradiography System .....	40
4. Ballistic Performance Summary .....	41
5. Port Diameters Measured by AEDC and UTSI on Motor No. 5 .....	42
6. Experimental Values of Base Burn-Rate Constants ( $r_o = cp^n$ ) .....	42

## 1.0 INTRODUCTION

A solid-propellant rocket motor (SRM) is designed to produce a total impulse and prescribed thrust versus time to fulfill its mission. This is accomplished by coupling the propellant grain characteristics with nozzle performance. The principal characteristics of a propellant grain are its surface burning rate and geometry. The ability to determine the burning rate of a solid propellant is of primary importance in the design of an SRM because the thrust/time curve depends upon this parameter. Unfortunately, theoretical knowledge of burning phenomena and accurate experimental propellant burn-rate data are inadequate so that the thrust/time curve of a new solid-propellant rocket motor must be determined from the full-scale firing of the rocket motors.

In view of the concern in the solid-propellant rocket motor industry of the present inability to measure in-situ propellant burning rates, a program was undertaken by Arnold Engineering Development Center (AEDC) and the Air Force Rocket Propulsion Laboratory (AFRPL) to develop a better method for propellant burn-rate determination. A new, noninterference test technique has been developed at AEDC which allows the average propellant burn rate to be determined over much shorter time periods than previously possible. This method, termed "X-ray flash cineradiography," combines a flash X-ray source with synchronized film changer and allows a maximum of six radiographs to be taken per second, delineating the propellant surface. The method was first applied to an end-burning solid gas generator (Ref. 1), where the objective was to observe burning behavior effects on chamber pressure. Measurement of the burn rate in that study was a secondary goal. In the present study, propellant burn-rate measurement was the main objective, and data were gathered for a series of six Hercules solid-propellant model rocket motors tested at sea-level-static conditions.

The goals of this program were to develop a method of accurately measuring directly from radiographs, flash-to-flash port diameter changes for a center-perforated propellant grain and to develop methods of determining the propellant burn rate. In order to fully validate the capability of this method, four of the six motors were designed to exhibit some degree of erosive burning in the port. It has been observed that this burn-rate anomaly leads to a faster burn rate in the nozzle end of the grain than at the forward (closed) end caused by the higher velocity at the exhaust end.

In addition to the flash cineradiographic technique for burn-rate measurements, motor performance measurements (chamber pressure, thrust, and motor case strain) were made on each of the tests. The burn-rate measurements obtained with this method will be compared with the motor performance data.

## 2.0 DISCUSSION OF SOLID-PROPELLANT COMBUSTION

### 2.1 BURN-RATE MEASUREMENTS

Accurate measurement of propellant burn rate is difficult. Various methods have been used such as interrupted burning, pressure curve analysis, pressure tap pickup, and radiographic inspection. All of these techniques result in the calculation of an "average" burn rate when the actual burn rate may vary considerably during the time of investigation. These methods will be discussed briefly.

1. **Interrupted Burning**—This method involves burning several propellants starting with the same initial conditions and abruptly terminating the burn at predetermined times after ignition. The web thickness of each propellant is carefully measured before the burn and then again after the burn is interrupted. The average burn rate for each individual propellant is the difference in web thickness divided by the time of burn. Several propellant samples are required to determine the burn rate as a function of time. This technique yields average burn-rate data and is attractive because the data are obtained under realistic operating conditions. One source of error is the uncertainty in the time taken to quench the surface combustion (Refs. 2 and 3).

2. **Pressure Curve Analysis**—This technique also yields average burn-rate data under realistic operating conditions. Internal ballistics theory is applied to the measured pressure/ time curve to obtain the average burning rate. Local or instantaneous values of burn rate are not possible with this technique, but the experimental setup is relatively simple. The principal source of error in this technique is the validity of the theoretical model used and lack of knowledge of the products of combustion and their gas properties (Ref. 4).

3. **Pressure Tap Pickup**—In this technique, pressure transducers are connected to pressure taps located at different known depths in the sample of propellant. When the propellant surface burns away to the point where the pressure tap is exposed, the pressure will increase. The propellant burn rate is calculated from the known distances between the pressure taps and the time interval between pressure change indications. The accuracy of the method depends upon accurately determining the location of the pressure taps and the time response of the transducers and data system (Ref. 2).

4. **Radiographic Inspection**—The flash cineradiography technique, such as that used for these tests, employs a flash X-ray system to "freeze" the port geometry at different times and obtain the mean burning rate from differences in those geometries. This approach allows direct measurement of average burning rates over relatively "small" time intervals

during the burn while maintaining realistic operating conditions. This procedure is appropriate for cylindrically perforated (CP) or end-burning grains. This method allows the measurement of port area from which the burn rate can be calculated as function of time and axial position in the motor. The time between data points can be significantly shorter than with the other methods, and the surfaces are frozen in time. Local burn rates at various positions along the surface are possible with this approach. The disadvantage of this approach is the complexity of making accurate measurements from radiographs.

## 2.2 BURN-RATE CHARACTERISTICS

The burn rate of an SRM is a complex function of the following variables: chamber pressure, flow velocity, grain temperature, propellant formulation, processing, and motor configuration. This report deals mainly with the first two factors.

For a cylindrically perforated SRM, propellant burn rate,  $r$ , is defined as

$$r = \Delta R / \Delta t \quad (1)$$

where  $R$  is the radius of the port. The true instantaneous burn rate at time,  $t$ , is given by

$$r_t = \lim_{\Delta t \rightarrow 0} \Delta R / \Delta t = dR / dt \quad (2)$$

The average burning rate would normally be computed from Eq. (1) when  $\Delta t$  is on the order of the motor burn time. For the tests reported herein,  $\Delta t$  was an order of magnitude less than motor burn time; therefore, the average value of the burning rate measured over this time interval might be termed "short-time" mean burning rate.

The influence of pressure on the linear or base burning rate can be expressed by St. Robert's law (Ref. 5) as

$$r_o = cp^n \quad (3)$$

where  $r_o$  is the linear burning rate,  $p$  is the combustion pressure, and  $c$  and  $n$  are constants determined experimentally for a given propellant. The parameter,  $c$ , is grain composition and initial temperature sensitive, whereas the index,  $n$ , is composition sensitive. This relationship has been found to be very accurate over the range of pressures generated during these tests. St. Robert's law assumes that burning proceeds normally to the surface. It has been observed that under certain conditions, the burning rate can be affected by the cross-flow velocity of the combustion gases past the burning surface.

For most applications, an SRM is designed to operate with a substantially constant chamber pressure. It is also desired that the loading density of the SRM be as large as possible. This is achieved by reducing the port-to-throat area ratio. A reduced port-to-throat area ratio results in a large flow velocity of the combustion gases past the burning surface of the propellant. This flow velocity often causes a significant change in the burning rate of the propellant; this phenomena has been termed "erosive burning." This increase in burn rate occurs in the early stages of the propellant burn for most motor configurations. Erosive burning can drastically alter the rate of propellant consumption, the initial chamber pressure, and the motor burn time. Therefore, it is difficult to predict accurately the quantitative effects of erosive burning on motor specific impulse.

It is evident that St. Robert's law must be modified to include the effect of cross-flow velocity on the burn rate. Many investigators have studied the effects of erosive burning using a variety of experimental methods and have developed expressions for the total burning rate. A typical example of the empirical erosive burning correlation was developed by Geckler (Ref. 6) as

$$r = r_o (1 + kG) \quad (4)$$

where  $G$  is the mass velocity and  $k$  is the empirical proportionality constant used to correlate data.

There is a lack of agreement among investigators regarding the characteristics of erosive burning. Propellants with a high burning rate were observed to be less erosive than slow-burning propellants. When the propellant burns to the point where  $A_t/A_p$  is less than one, erosive burning decreases. Erosive burning was observed to be higher at the nozzle end of the port than at the forward end (Ref. 2).

### 3.0 TEST DESCRIPTION

#### 3.1 TEST ARTICLE DESCRIPTION

The motors used for these tests were designed and built by Hercules, Inc., Allegheny Ballistics Laboratory. The motor configuration (Fig. 1) consisted of a cylindrical graphite case with forward and aft steel closures. The forward closure contained an igniter chamber and pressure port. The aft closure also had a pressure port and a pressure-relief assembly held in place with four aluminum pins designed to shear at a chamber pressure of 4,000 psia. The aft closure included an internal nozzle consisting of replaceable graphite throat and midsection inserts with the 6-deg exit cone as an integral part of the pressure-relief closure. The 86-percent ammonium-perchlorate-based propellant (Table I) was precast in cellulose

acetate cylinders and included a circular center bore. The degree of erosive burning was controlled by a combination of the propellant bore and nozzle throat diameters. Table 2 lists the grain and nozzle geometries as a function of the expected burning characteristics. Two motors of each different grain configuration were tested. The purpose of the different designs was to investigate three different erosive burning levels and the associated pressure/time curves. After one of each type of grain configuration was tested, it appeared that the amount of erosive burning was much less than the manufacturer had predicted. However, the amount perceived and the ability to determine the actual degree of erosive burning was reduced because of end burning. The action of burning the grain from both ends reduced the length of the grain, thereby degrading perspective and eliminating reference points used to compute erosive burning. In an effort to counter these problems, the nozzle-end surface of one grain was inhibited. The manufacturer provided an epoxy to be applied to the exposed propellant surface in a layer approximately 0.060-in. thick. The propellant grain chosen was classified as highly erosive and was tested as Motor No. 5.

The motors were assembled by AEDC personnel prior to testing. Assembly procedures included installation of the igniter, insertion of the propellant cylinder and nozzle inserts, and closure installation. Motor case strain gages were applied and the pressure transducers were connected. Each motor was pressure checked with Freon® to insure proper sealing of the motor chamber. Pre- and posttest motor assembly weight, nozzle throat, and exit-plane diameter measurements were also recorded for each motor.

### **3.2 TEST FACILITY DESCRIPTION**

These motors were tested at AEDC during December 1983 and January 1984 at ambient, static conditions at the Ground-Level Test Stand (GLTS). This facility consists of a control room and an adjacent open-ended test bay and is adaptable to a wide variety of research and investigative test requirements. The motor installation (Fig. 2) included a flexure and motor support stand to isolate the motor and load cell from off-axis forces.

A digital, programmable controller was used to command the film-changer control system activation and motor-ignition events. Motor performance instrumentation included two chamber pressure transducers, an axial-thrust load cell, and three axial strain gages mounted at motor top-dead-center and spaced equidistant between the forward and aft closures.

Motor performance data were recorded on two systems. One system utilized a stand-alone microcomputer configured to sample each of ten data channels at 1,000 samples/sec. Raw data were recorded on magnetic tape immediately after acquisition was complete and later reduced to engineering units using an identical system in the laboratory. This data

acquisition system was used to provide a quick-look capability between tests and as a backup for the primary system. The primary data acquisition system for these tests was a portable FM analog tape drive. The FM data were then digitized at 5,000 samples/sec. The raw digitized data were reduced to engineering units, tabulated, and plotted using a digital mainframe computer.

### 3.3 X-RAY SYSTEM DESCRIPTION

Figure 4 is a schematic of the cineradiographic recording system. The X-ray source is a Hewlett Packard (HP) 180-kv dual-channel X-ray system which consists of a pulse generator, high-voltage power supply, cold-cathode field emission X-ray tube, and associated controls. The 30-kv, 1-ma high-voltage power supply normally used with the unit was replaced with a Hipotronics 30-kv, 830-ma unit which has sufficient current capability for rapid charging of the pulse generator. Single radiographs are made using the HP power supply, and the Hipotronics power supply allows operation at rates up to 10 flashes per sec. Duration of the flash is on the order of 25 nsec, permitting high-speed events to be recorded without motion blur. Additional specifications of the cineradiographic system are given in Table 3.

X-ray film was used as the recording medium because of its resolution capabilities and availability. A Schonander, rapid-change, cut-film changer was synchronized with the operation of the flash X-ray tube. The changer has a maximum recording rate of six sheets per second and holds up to 30 sheets of 10- by 12-in. film. For these tests, 25 exposures (approximately 4 sec) were considered sufficient to cover the expected 2- to 3-sec motor burn. A program selector sets the rate of film change and the timing sequence. Individual films were sequentially imprinted with the exposure number, date, and test number. Figure 2 shows the X-ray source, test article, and film changer. The lead shields were used to reduce the amount of scattered radiation from the test installation. Scattered radiation degrades the quality of the radiographic image.

The X-ray system performance was monitored using a desktop microcomputer to record both the relative voltage of the X-ray pulses and the elapsed time between successive pulses as shown in Fig. 4. A pulse stretcher expanded the time duration of the 25-nsec X-ray voltage pulse to allow the peak-hold detector to acquire the pulse data. The microcomputer stored each pulse height and displayed the values for analysis.

### 4.0 RADIOGRAPHIC DATA REDUCTION

The direct approach to obtaining propellant burn rate from radiographs is to measure port diameters (for CP motors) directly from the radiographic image. The difference in port

diameters,  $\Delta d$ , between two successive radiographs yields an average burning rate over the finite time period,  $\Delta t$ , between X-ray flashes; i.e.,

$$r = \Delta d / 2 \Delta t \quad (5)$$

The accurate measurement of  $\Delta d$  is difficult. The burning propellant surface may be highly irregular. In addition to this, images on X-ray film are blurred because of inherent factors present in the image-forming process. Another major problem concerns the assumption of port symmetry during the burn. The direct approach cannot account for anomalous burning and noncircular ports. The techniques discussed in this section were developed to overcome these limitations.

#### 4.1 AFRPL DATA REDUCTION METHOD

The method developed by H. M. Pressley, Jr. and R. L. Glick features direct measurement of total port area (mass burning rate is determined directly). In this method, improved accuracy over port diameter measurement is intended by eliminating the distance measurement, which may be subjective, and by integrating the film-density data to attenuate random radiographic errors. Film-density data across the entire bore region of the radiograph contains information relative to not only the local diameter (assuming symmetry), but also the true nature of the port geometry and cross-sectional area (assuming nonsymmetry).

A computer model of the X-ray process begins with Beer's law

$$I = I_0 \exp(-\mu_m \rho t) \quad (6)$$

where

- $I$  = Intensity of Emerging Beam
- $I_0$  = Intensity of Incident Beam
- $\mu_m$  = Mass Absorption Coefficient of the Material
- $\rho$  = Material Density
- $t$  = Object Thickness

Assuming that  $I$ ,  $I_0$ ,  $\mu_m$ , and  $\rho$  are known for a beam passing through a CP motor, the remaining parameter, thickness, can be determined. The approach developed by Pressley and Glick to compute port cross-sectional area uses a ray-tracing process. A brief, simplified description of this process is as follows:

The total motor thickness,  $t_m$ , is

$$t_m = t_c + t_p + t_v \quad (7)$$

where

$$\begin{aligned} t_c &= \text{Case Thickness} \\ t_p &= \text{Propellant Thickness} \\ t_v &= \text{Port Thickness} \end{aligned}$$

The case thickness,  $t_c$ , can be determined from motor case dimensions and setup geometry. Propellant thickness comes from Beer's law for the simple CP motor

$$I = I_0 \exp - (\mu_{mc} \rho_c t_c + \mu_{mp} \rho_p t_p) \quad (8)$$

The port thickness,  $t_v$ , comes from Eq. (7), but recall that the objective is to determine port cross-sectional area. To do this, consider the rays emanating from a point source which pass through the port region from  $z_1$  to  $z_2$  (Fig. 5). For each ray,  $t_v$  is computed from Eqs. (7) and (8). Port area  $A_p$  is computed from the summation of the rays

$$A_p = \sum_{i=1}^n t_{vi} \Delta z_i \quad (9)$$

where  $n$  is the number of measured increments from  $z_1$  to  $z_2$ . Solution of Eq. (8) is critical to obtaining an accurate value for  $t_v$ .

The advantage of this procedure is that the ray-tracing process computes the total port region and can be used for any port shape (CP, star, wagon wheel, etc.). The summation process tends to cancel errors in individual intensity measurements. The accuracy of this technique for calculating port area is dependent upon the size of  $\Delta z$  and the degree of irregularity of the propellant surface around the port perimeter.

## 4.2 UTSI DATA REDUCTION METHOD

The method developed by Smith (Ref. 7) to measure port diameters of the SRM takes advantage of prior knowledge about the shape of the test article to improve the accuracy of measurement. The approach uses Beer's law to develop a model of the relative image-density variations. The diameter of the port region is varied in the model, and the cross-correlation of the model to the empirical data is calculated. The cross-correlation value is assumed to be maximum when the input diameter matches that of the data.

The method is developed around a simple hollow cylinder. First, a simple ideal image, based on Beer's law attenuation, is calculated and then degraded to account for the reduction of image contrast caused by scattering and blurring attributable to the finite source size and the intensifying screens. The resulting degraded image-density values are

then transformed to account for the nonlinear recording characteristics of radiographic film.

Quantitative evaluation of the model was obtained by applying the method to the measurement of the inner hole diameter of a hollow plastic cylinder of known dimensions. A radiograph of the cylinder was digitized, and measurements were performed for 200 separate scan lines taken at different axial positions along the cylinder. These measurements yielded values of the inner hole radius ranging from 1.747 to 1.798 cm with a mean of 1.7776, a mode of 1.772, and a standard deviation of  $\pm 0.01189$ . These values can be compared with the machinist's measured value of 1.7770 cm for the cylinder. The cross-correlation values for the actual and theoretical images ranged from 0.9979 to 0.9989 for the 200 scans with a mean of 0.9984. For the test data, the model for the simple hollow cylinder was modified to include the cellulose acetate insulation around the propellant and the graphite-epoxy motor case.

### 4.3 AEDC DATA REDUCTION METHOD

The X-ray radiographs obtained during the tests were analyzed with the aid of an EYECOM Spatial Data Systems Image Analyzer. In this system, the picture is divided into a pixel array of 640 horizontal columns and 480 vertical rows, producing 307,200 equal and discrete picture elements (pixels). Each pixel is then assigned a value based on the measured level of gray contained on that portion of the picture which it encompasses. The gray scale, or  $z$  values of the pixels, ranges from 0 to 255, where 0 is black and 255 is white. Of the various edge-enhancing routines available on the EYECOM, the gradient routine was found to be the most efficient for the low-contrast, high-noise images found on radiographs.

Consider the density distribution predicted by Beer's law for a hollow cylinder as shown in Fig. 6. When the degradation mechanism of penumbra, screen/film effects, and Compton scatter area added to this model (Ref. 7), the predicted intensity profile is shown in Fig. 7. The cusps on these profiles indicate the regions in the cylinder where the material is the thickest (greatest amount of attenuation). In the ideal image, the cusps would pinpoint precisely the tangential point of the X-ray beam and inner surface of the cylinder. Thus, the boundaries of the inner core could be measured directly. However, because of the effects of degradation in the image-forming process, these sharp points are rounded and also appear to be displaced a small amount (outward from the center). Blurring and degradation effects make determining the location of the surface of the inner diameter of the cylinder a more difficult problem. Using the cusps as the location of the cylinder edges would give an erroneously large value for the inner diameter.

In terms of a digitized image, an edge is defined as an area of rapid change in gray level (film density) between two or more picture elements. For radiographs, this change is not

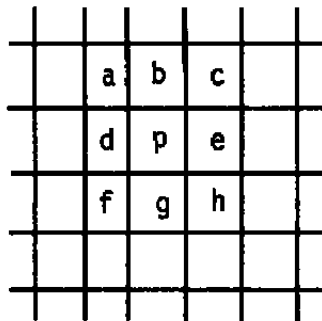
instantaneous, but is spread out over many pixels because of the image degrading effects. The magnitude of the gradient,  $G$ , at pixel location  $(x, y)$  is defined as

$$G = \sqrt{\left(\frac{\partial z}{\partial x}\right)^2 + \left(\frac{\partial z}{\partial y}\right)^2} \quad (10)$$

where  $z$  is the gray level. The EYECOM system software approximates the magnitude of the gradient at each pixel,  $p$ , from the pixels surrounding it by the following

$$G = |(f + g + h) - (a + b + c)| + |(c + e + h) - (a + d + f)| \quad (11)$$

where the letters indicate neighboring pixels surrounding the pixel of interest as defined by the following array:



This is an example of a 3 by 3 mask, or template, operating on the gray level of the pixels inside the mask. The first absolute value represents the estimate of the derivative in the  $x$  direction, and the second absolute value represents an estimate of the derivative in the  $y$  direction. The center of the mask,  $p$ , is moved around the image from pixel to pixel, computing the derivatives at each point. The gradient represents the rate of change of gray levels across the picture, and the edges can be assumed to be located at the point of maximum rate of change of gray level.

Applying the gradient edge-enhancing routine to an image results in another picture in which all edges are portrayed as white (high  $z$  value) lines against a black (low  $z$  value) background. Since random noise on the radiograph can cause spikes not associated with an edge, a sliding average in the  $x$  direction was applied after the gradient program was run to smooth out any effects of noise. A peak-locating program was applied after the edge enhancement and smoothing routines to locate the edges. Figure 8 shows a composite plot of the density distribution of a hollow cylinder and the  $g$  gradient routine applied to it. Note that the maximum gradient locations are inside the apparent inner-edge locations.

The gradient technique picks the edge location to the nearest pixel; therefore, the highest accuracy with this approach is to within one pixel. Pixel location of edges can be converted to absolute units when given the magnification factor of the radiograph. For these tests, typical values for the pixel size were on the order of 0.010 in. Applying this technique to a variety of radiographs of objects of known dimensions yielded percent errors ranging from 8 percent for poor quality radiographs to less than 1 percent for good images.

## 5.0 RESULTS

### 5.1 TEST SUMMARY

Six motors were successfully tested at the Ground-Level Test Stand between December 1983 and January 1984. The motor action times ranged from 2.24 to 3 sec, and the maximum chamber pressure ranged from 1,127 to 1,661 psia. The values of maximum thrust were 155 to 182 lbf. A motor performance summary for the tests is presented in Table 4.

Figure 9 summarizes chamber pressure and axial-thrust time histories for each of the six tests. The chamber pressure data presented are from the forward closure pressure tap. Data from the aft pressure tap were considered invalid after Test No. 2 because of tap clogging problems.

A typical plot of indicated case-strain and film-change events is shown in Fig. 10. The repetitive negative noise spikes in the data were caused by the X-ray system. These spikes were present in the FM data for all channels, but the strain gages were more susceptible because of their lack of built-in shielding. The charging voltages were very repeatable, varying by no more than 4 percent.

### 5.2 BURN-RATE DATA

Examples of burn-rate measurements made using the gradient edge-detecting routines, Method 3, are shown in Figs. 11 through 14. Burn-rate data from Test Nos. 1 and 4 are not included here because their configurations were similar to Motor Nos. 6 and 2, respectively. Test No. 6 (Fig. 11) is the baseline, no erosive burn motor. It can be seen that the burn rate is similar all along the axis of the motor. This motor experienced about 21-percent change in nozzle throat area during the burn. Test No. 2 was chosen for the mild erosive burn motor, although it had the largest nozzle erosion (50 percent) of any of the motors (Table 4). Nozzle erosion was responsible for the tail-off in the chamber pressure versus time for this motor. Evidence of erosive burning was seen by the more rapid burn rate in the nozzle end than at the center and forward-end locations. Figure 12 shows that the nozzle end attains a

high burn rate early in the burn and maintains it, whereas the center and forward end take slightly longer to reach the same burn rate.

Motor Nos. 3 and 5 were highly erosive burning motors with No. 5 having its nozzle end inhibited. Motor No. 3 (Figure 13) showed a higher erosive effect on the nozzle end than No. 5 (Fig. 14). The effect of the inhibitor increased the action time of Motor No. 5 to 2.996 sec, the longest of any motor tested. This motor also had the largest specific impulse of any motor tested. Motor No. 5 experienced greater nozzle erosion (21 percent) than Motor No. 3 (11 percent).

A plot of bore diameters versus axial position for each of the motors at about two-thirds through the burn is shown in Fig. 15. It can be seen that Motor No. 6 (no erosive burn) has about the same inner diameter from nozzle to forward end. The other motors (Nos. 2, 3, and 5) show more rapid burning at the nozzle end. The dramatic curve for Motor No. 2 may be attributable to the rapidly eroding nozzle allowing erosive burning to continue longer than it normally would. Motor No. 5 experienced a slightly higher burn rate on the forward end as well as the nozzle end (compared to the center). This may have been attributable to the effect of the inhibitor on the nozzle.

Burn-rate measurements are not yet available for the AFRPL technique. Application of this technique to selected radiographic data indicated that actual film-density data and computed data yielded excellent correlation. Port cross-sectional area computations along a port of known size resulted in errors of less than 1 percent. Burn-rate measurements obtained from Method 2 are compared with the burn rate measured by Method 3 in Fig. 16. These data are for Motor No. 5. Port diameters measured by the two different techniques are listed in Table 5.

Of the observed characteristics of erosive burning discussed previously, the port geometry effect was the most dramatic in these tests. Motors designed for erosive burning showed a higher burn rate at the nozzle end than at other points on the axis. It was also observed that motors designed for erosive burning had a longer action time.

The burn-rate values obtained by Method 3 were combined with the measured chamber pressures to obtain values for the constants in St. Robert's burn-rate equation,  $r_0 = cp^n$ . These experimental values are presented in Table 6. All values were calculated from measured burn-rate data at the head end of each of the four motors.

The motor manufacturer, Hercules Incorporated, computed performance prediction for each of the three types of motor configurations. Predicted chamber pressures are shown in Figs. 17, 18, and 19, together with the measured chamber pressures. Discrepancies between predicted and measured performance can be explained by temperature effects, excessive

nozzle throat erosion (especially in the mild erosive case), and suspected emission of burning particles instead of smooth combustion. Further theoretical analyses of these motors will be made here at AEDC.

### **5.3 BURN ANOMALIES**

Some of the more interesting results of these tests were not measurable, but observed burning anomalies were revealed in the radiographs. Pits and craters attributable to propellant voids or localized irregular burning were seen in some of the radiographs. One of the largest was 10 mm (0.4 in.) in diameter and 2.5-mm (0.1-in.) deep. The radiographs revealed that in three of the six motors, the port centerline was offset. It was speculated that mandrels used to form the ports of these three grains were apparently not centered during the propellant pour and cure processes. During the burn, the thinner part of the web was seen to disappear first. The cross-correlation method (Method 2) has to be modified to deal with this peculiarity.

All of the motors except No. 5 were designed to permit burning at both ends. The radiographs revealed that the forward end burned evenly, as it should for pressure-dependent burning, but anomalous burning was seen on the nozzle end of the grain. Pressley and Glick have analyzed this phenomena and have concluded that this anomalous burning was "erosive burning resulting from vortex flow in the cavity formed by the end of the grain and the base of the nozzle housing. Later radiographs showed that as the cavity widened, this erosive burning ceased and the surfaces lost most of their irregular shape."

The inhibitor applied to Motor No. 5 failed approximately 1.3 sec into the burn. Analysis of the measured burn-rate, pressure, and thrust curves all showed a rapid rise at this point. Burn anomalies which had been observed on the nozzle-end grain of the other motors appeared at this time, but were much more severe. The inhibitor appeared to have become completely detached from the grain at about 2.3 sec into the burn and was expelled through the nozzle. Examination of photographs made during the test showed relatively large particles being expelled at approximately this time. No trace of the inhibitor was found in the motor casing after postfire. Inhibitor breakdown is offered as the explanation for the spikes in the pressure and thrust curves for Motor No. 5.

### **6.0 CONCLUSION**

This test project provided experimental data for the measurement of solid-propellant burn-rate and motor ballistic performance. The goals of this program were to develop a method of making accurate measurements directly from radiographs, and to use these measurements to calculate the propellant burn rate of a center-perforated grain. Flash

radiographs of the burning propellant surface were recorded during six rocket motor tests. This technique offers the advantages of realistic operating conditions and higher data rates than other measurement techniques. Three different burn-rate-measurement approaches were developed to analyze the radiographic film data.

The first method improves accuracy by integrating the film-density data to attenuate random radiographic errors. This approach overcomes some of the inherent problems and limitations involved in obtaining accurate measurements from radiographs, works well on nonsymmetrical ports, and can be used for any port shape. Burn-rate calculations obtained by this approach are not yet available for publication.

In Method 2 a mathematical model of the X-ray image of the test article was computed, and the best cross-correlation of the calculated model with the actual image was used to determine the best value for the port diameter. On a hollow cylinder of known dimension, this technique yielded port diameters to within 6  $\mu\text{m}$  of the true values. Burn-rate measurements made using this approach are included in Section 5. This technique can be modified for test article configurations other than CP.

The third approach uses edge-detecting software to measure propellant bore diameters. Measurement accuracy is to one pixel (0.010 in. for these tests). The advantage of this technique is that it requires a minimum of information about the object radiographed. It does not require knowledge of the X-ray beam energies, scattering effects, fluorescent screen blurring, or film nonlinearities. Burn-rate measurements obtained with this method are given in Section 5 for comparison with Method 2.

Motor chamber pressures predicted by the manufacturer were included for comparison with the measured pressures and calculated burn rates. In addition to the quantitative data obtained, some interesting burn anomalies were observed from the radiographs.

## REFERENCES

1. Walker, R. Y. et al. "X-Ray Cineradiography Applications to Rocket Testing." 20th JANNAF Combustion Conference, Monterey, California, October 1983.
2. Marklund, T. and Lake, A. "Experimental Investigation of Propellant Erosion." *ARS Journal*, Vol 3, No. 2, 1960, pp. 173-178.
3. Brooks, W. T. "Workshop Report: Burn Rate Determination Methodology." 18th JANNAF Combustion Meeting, JPL, Pasadena, California, October 1981.

4. Parkinson, R. C. and Penny, P. D. "A Transpired Boundary-Layer Model of Erosive Burning." AIAA/SAE 14th Joint Propulsion Conference, July 1978.
5. Sutton, G. P. *Rocket Propulsion Elements*. Third Edition, John Wiley and Sons, Inc., New York, 1963.
6. Geckler, R. D. "The Mechanisms of Combustion of Solid Propellants." AGARD Publication 1470, *Selected Combustion Problems*, Proceedings of the First AGARD Combustion and Propulsion Colloquim, Butterworth Scientific Publications, London, 1954, pp. 283-339.
7. Smith, L. M. "A Model for Image Formation in X-Ray Radiography." Master's Thesis, University of Tennessee, June 1984.

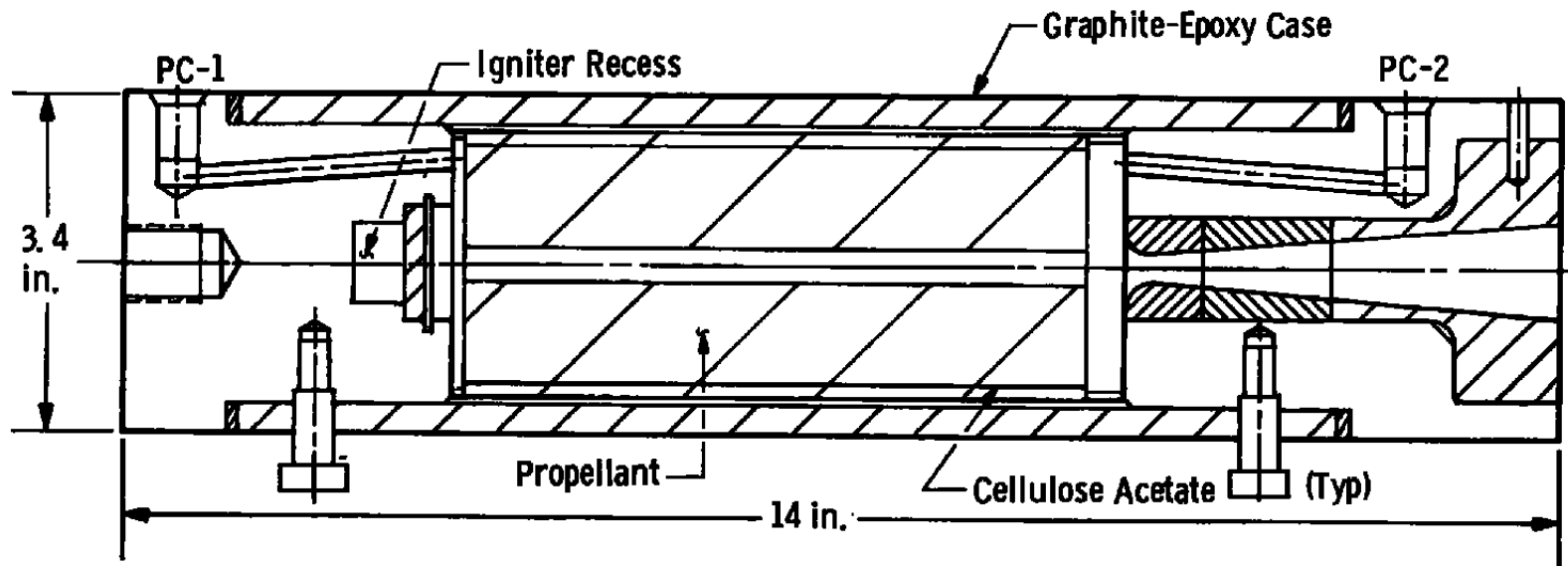


Figure 1. Test article configuration.

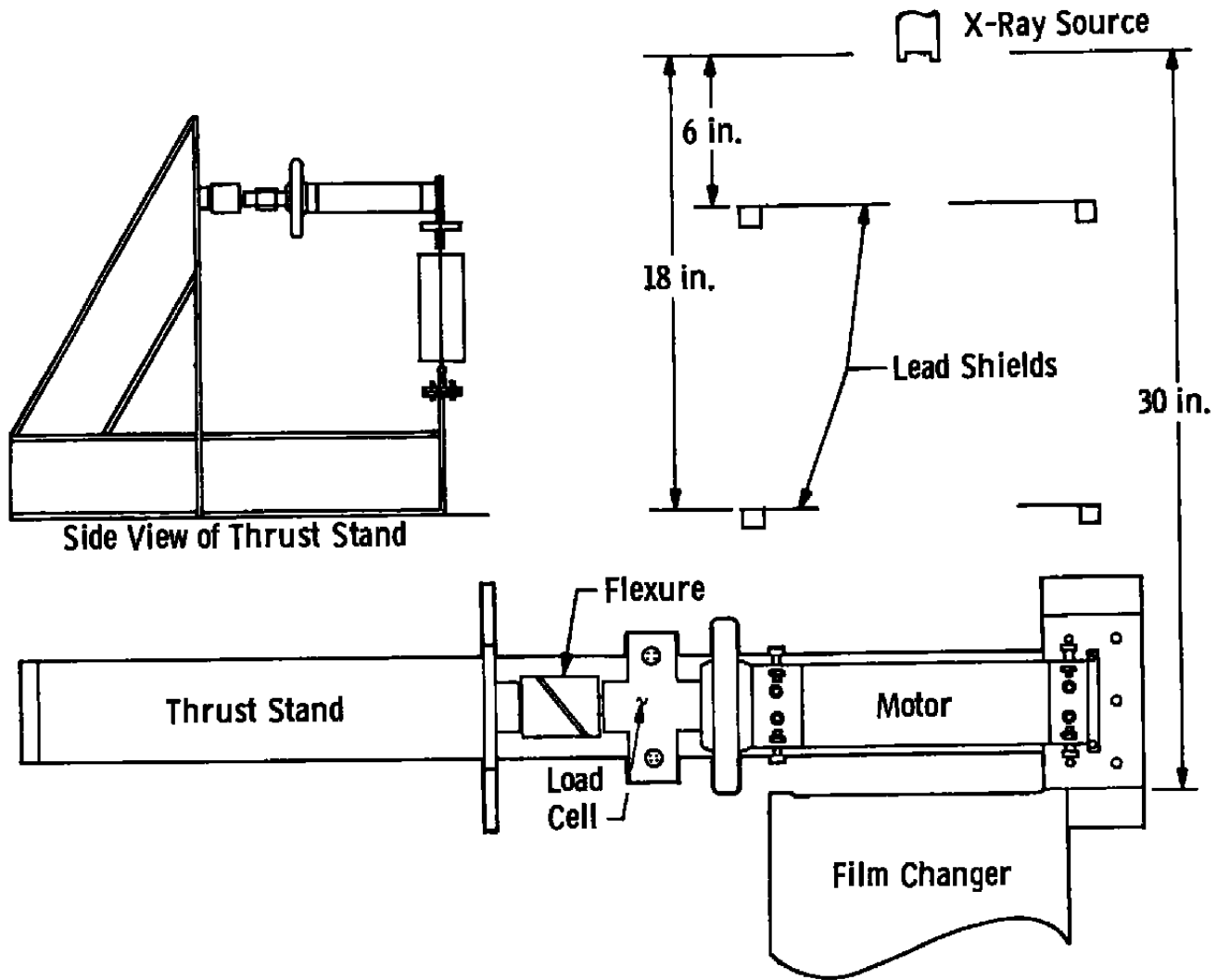


Figure 2. Test installation.

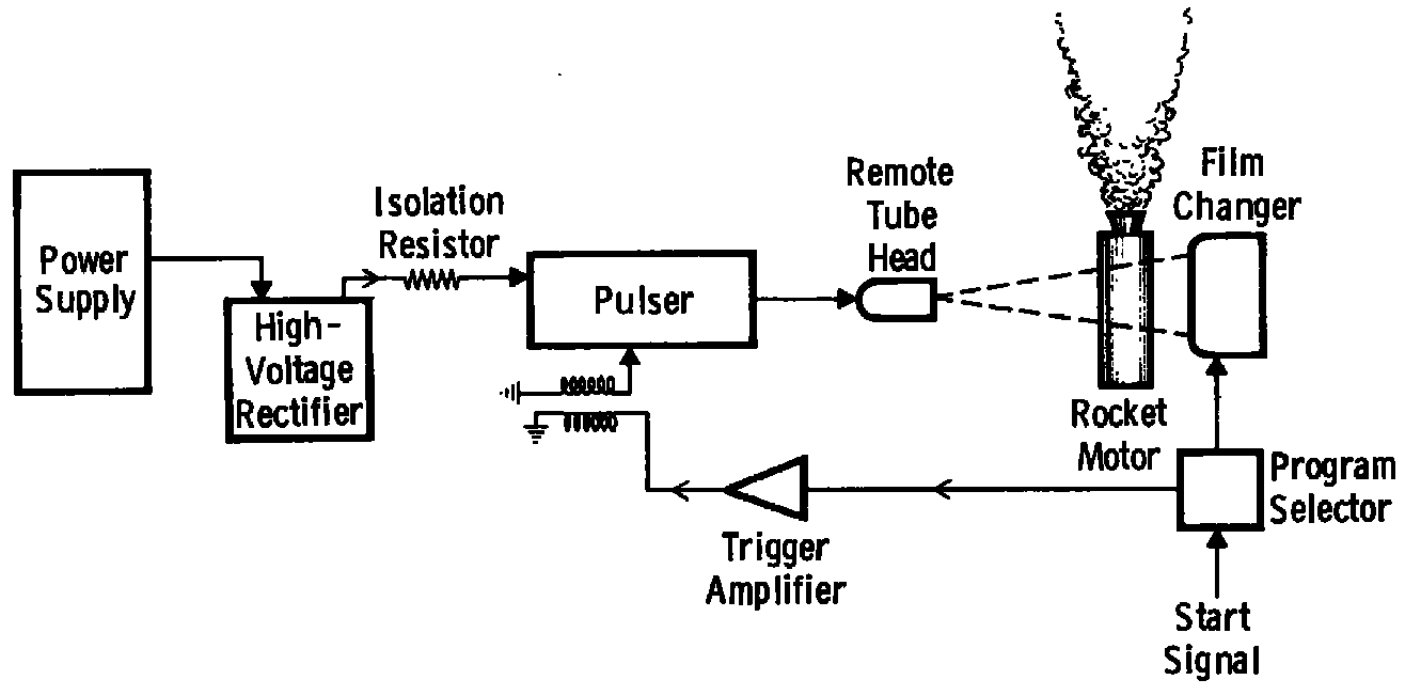


Figure 3. X-Ray cineradiography system.

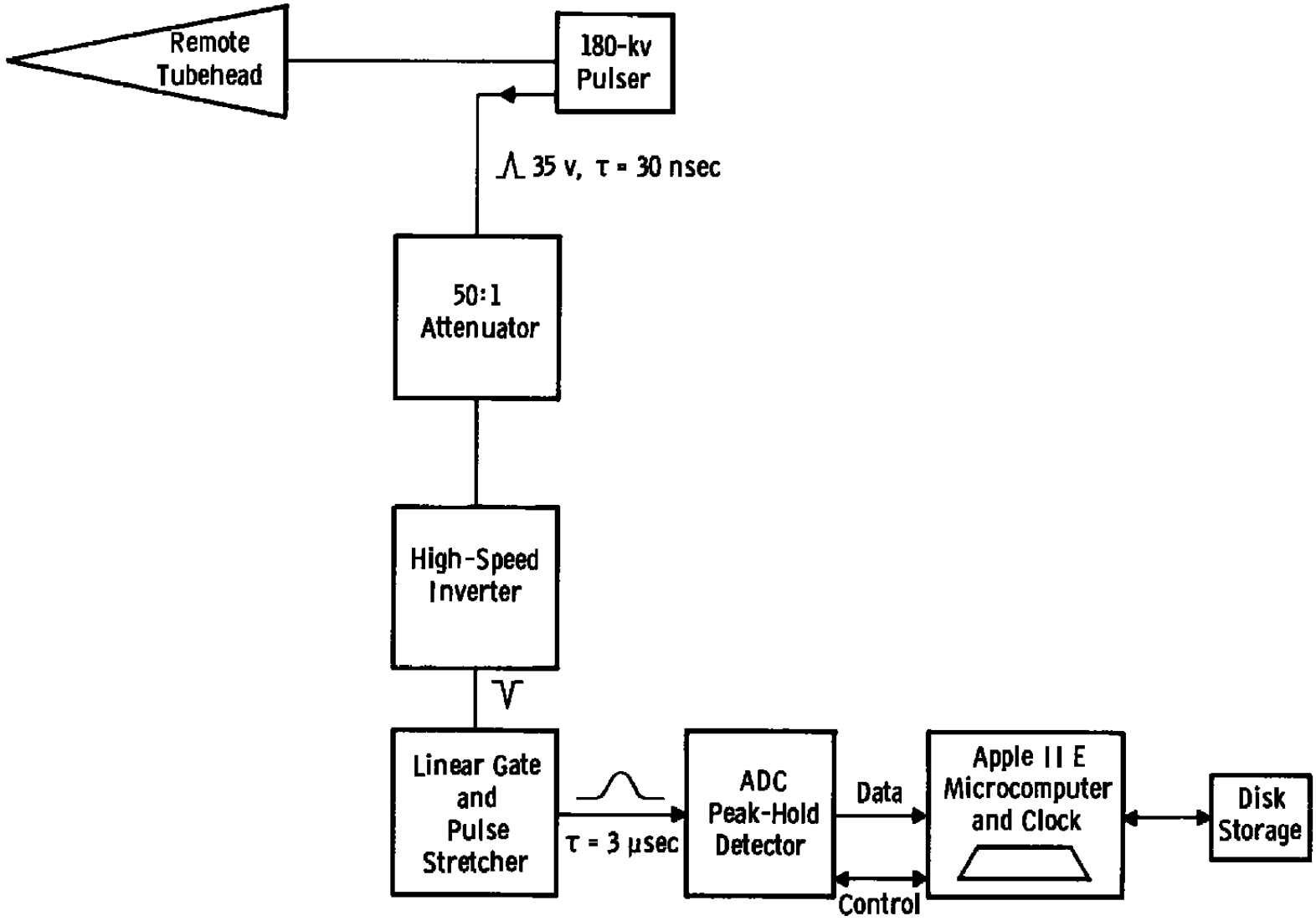


Figure 4. System for monitoring pulser output.

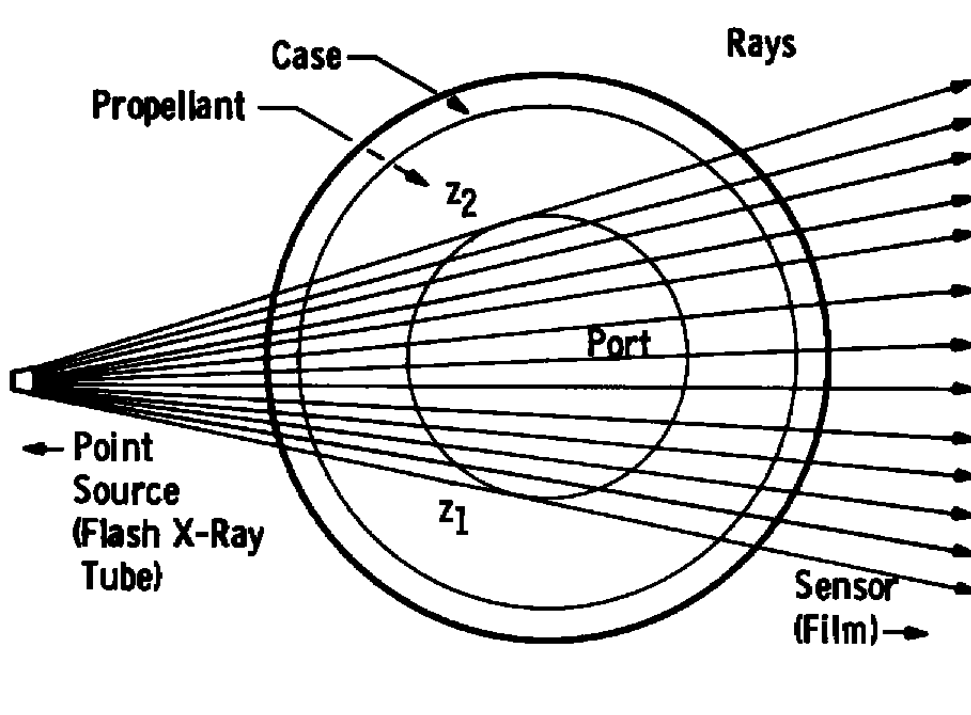


Figure 5. Ray-tracing process to compute port area.

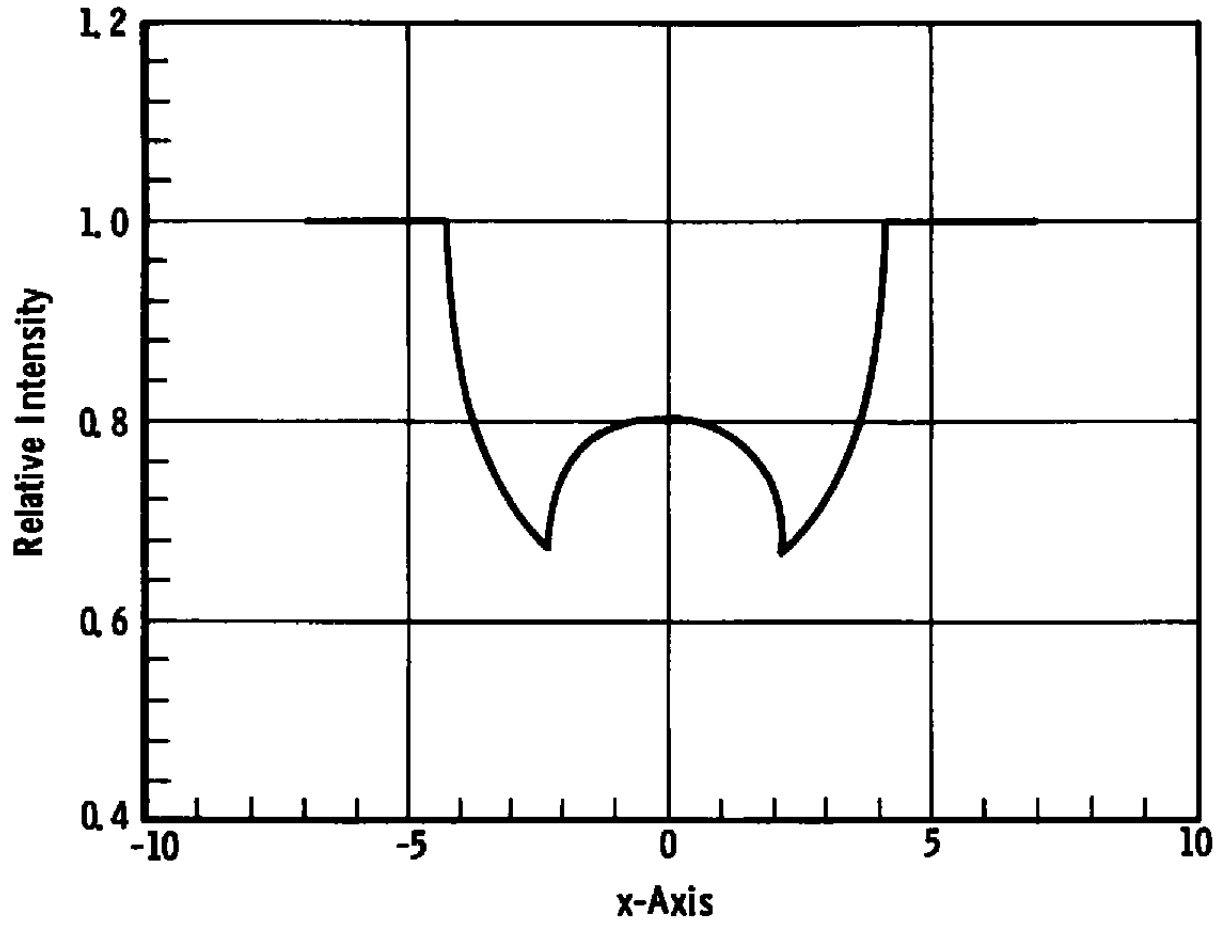


Figure 6. One-dimensional ideal image for cylinder.

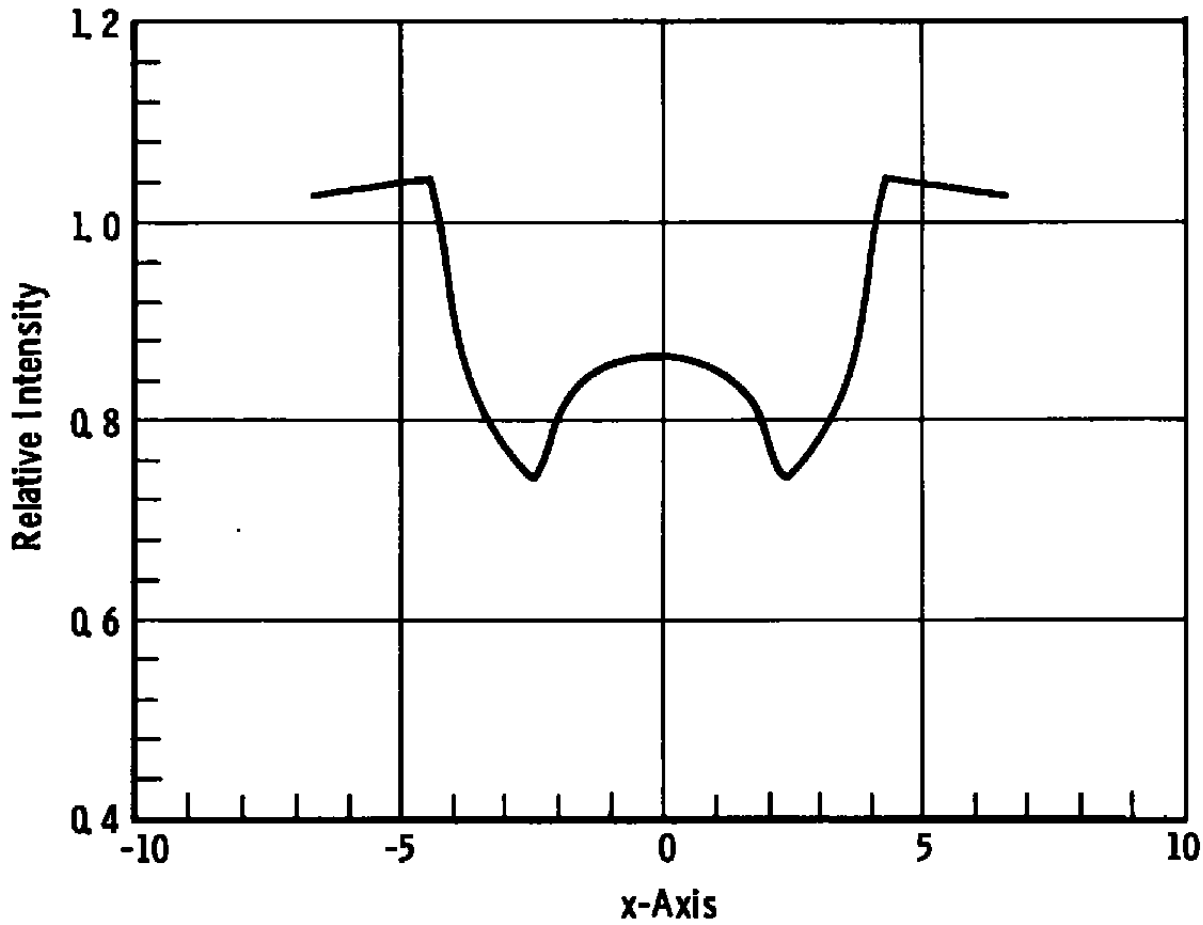


Figure 7. One-dimensional degraded image for cylinder.

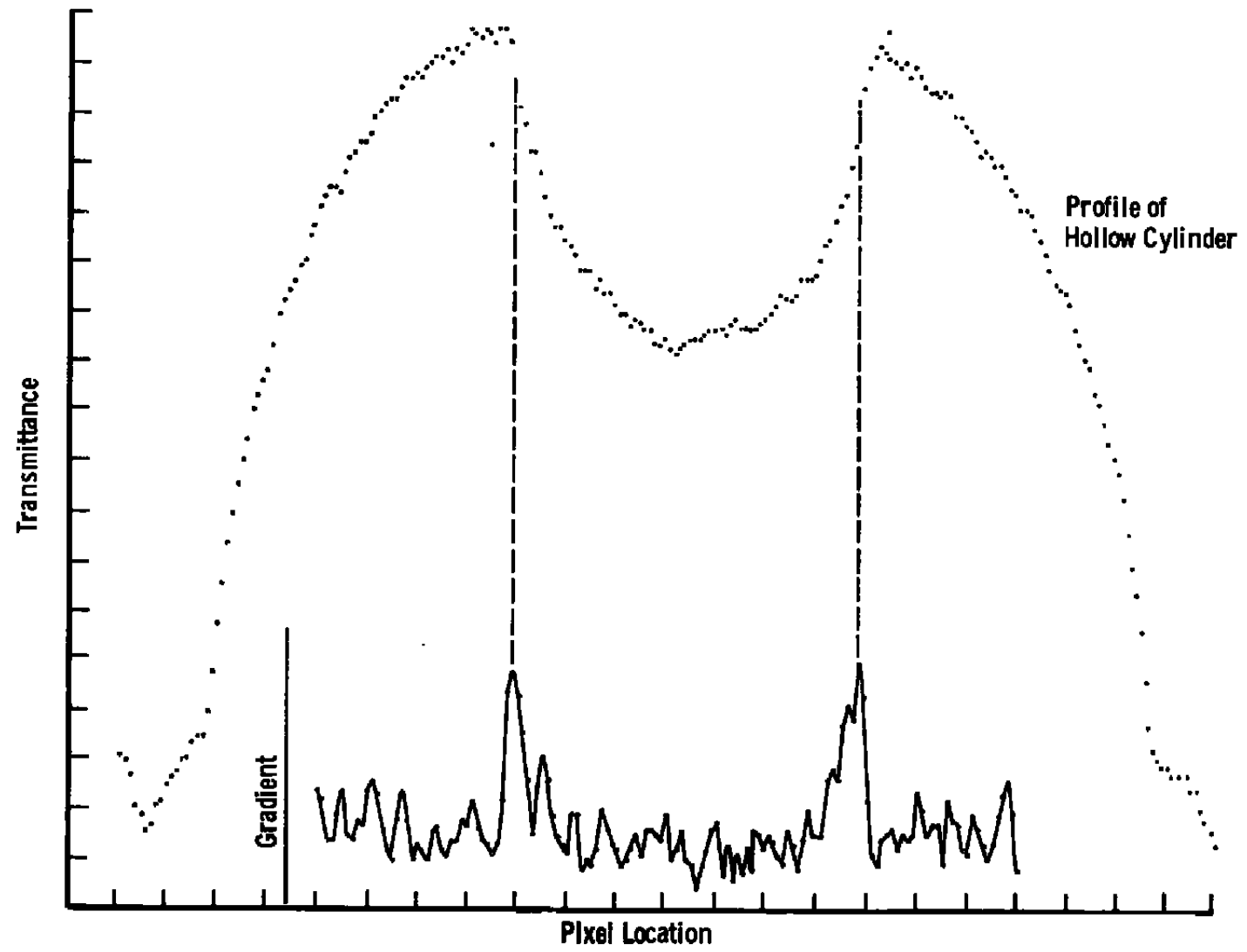
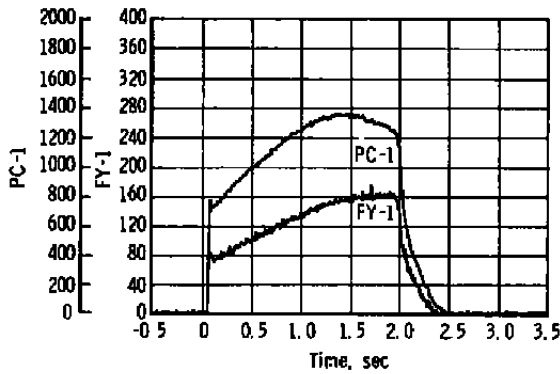
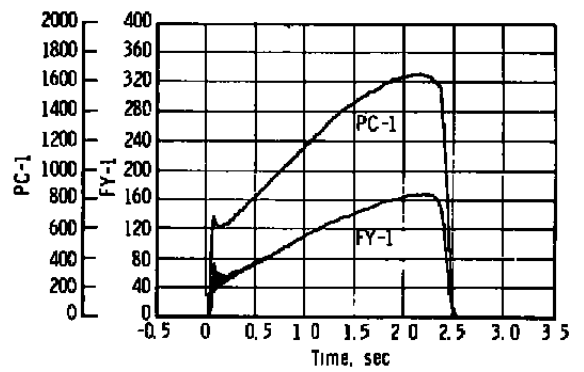


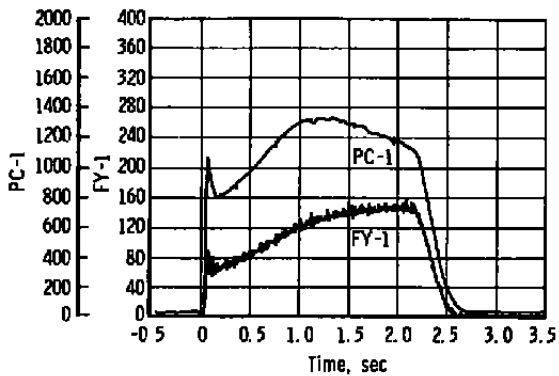
Figure 8. Density distribution of a hollow cylinder and gradient.



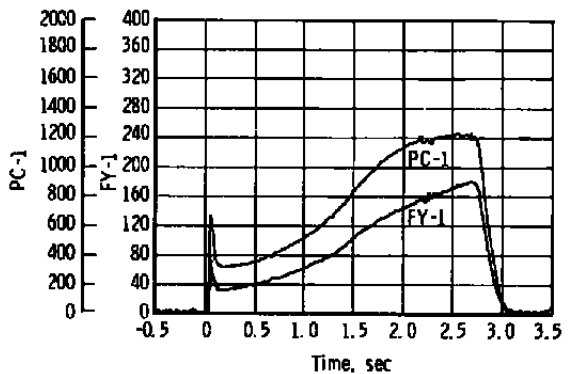
a. Motor No. 1 (no erosive burn)



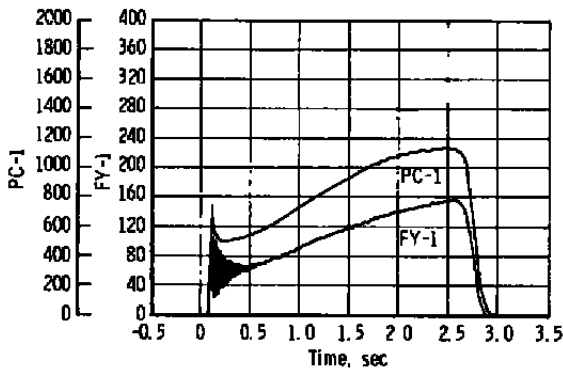
d. Motor No. 4 (mild erosive burn)



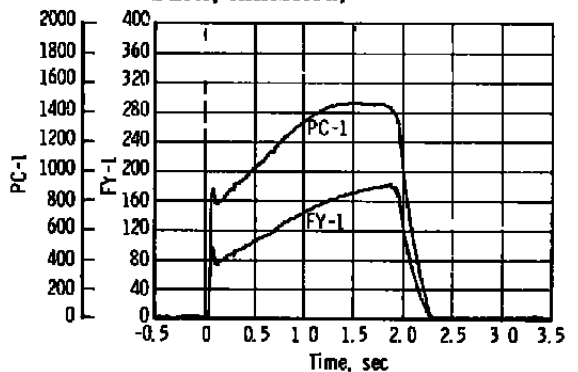
b. Motor No. 2 (mild erosive burn)



e. Motor No. 5 (high erosive burn, inhibited)



c. Motor No. 3 (high erosive burn)



f. Motor No. 6 (no erosive burn)

Figure 9. Chamber-pressure and axial-thrust time histories.

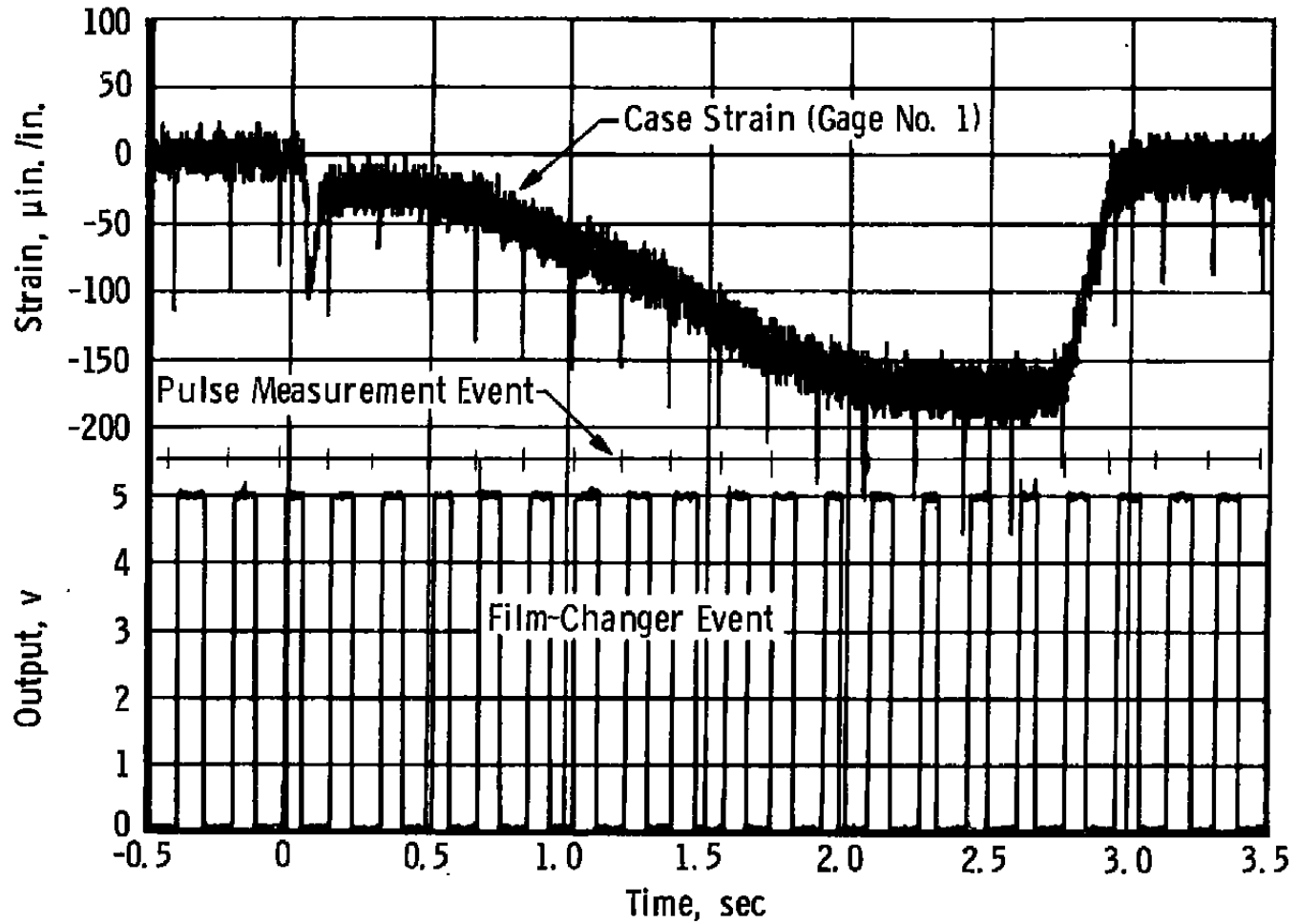


Figure 10. Case strain and film-change event.

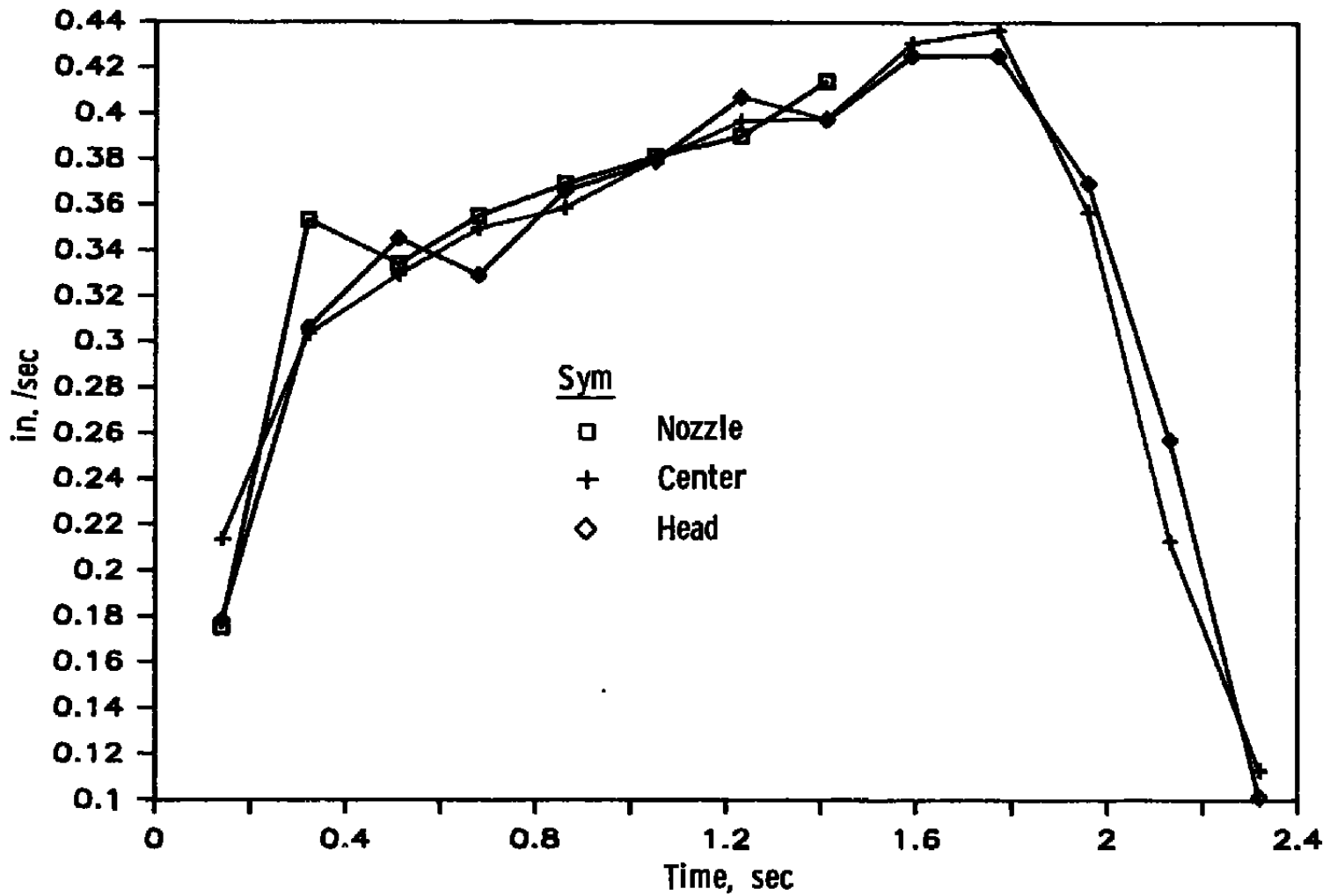


Figure 11. Burn-rate measurement, Motor No. 6.

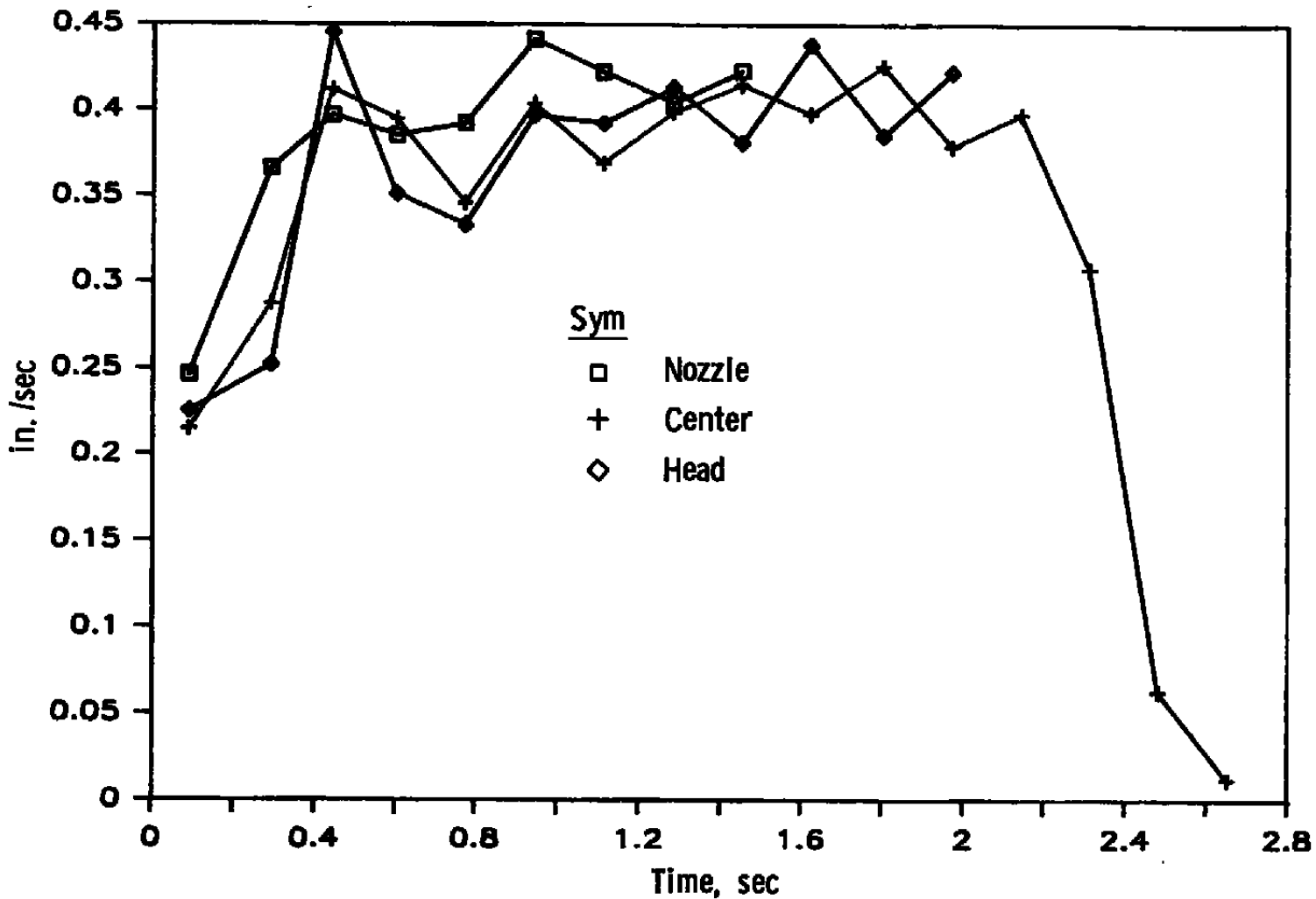


Figure 12. Burn-rate measurement, Motor No. 2.

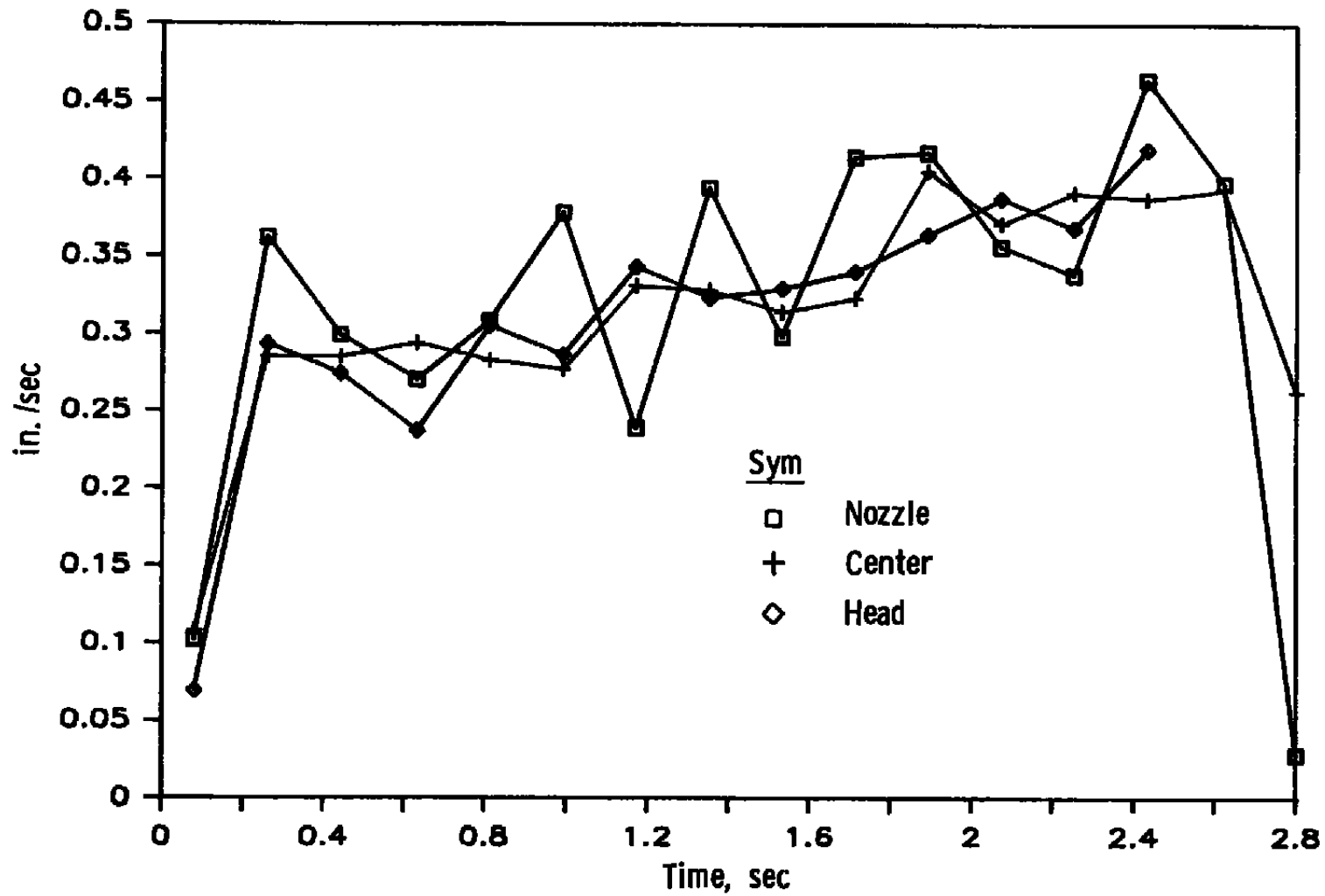


Figure 13. Burn-rate measurement, Motor No. 3.

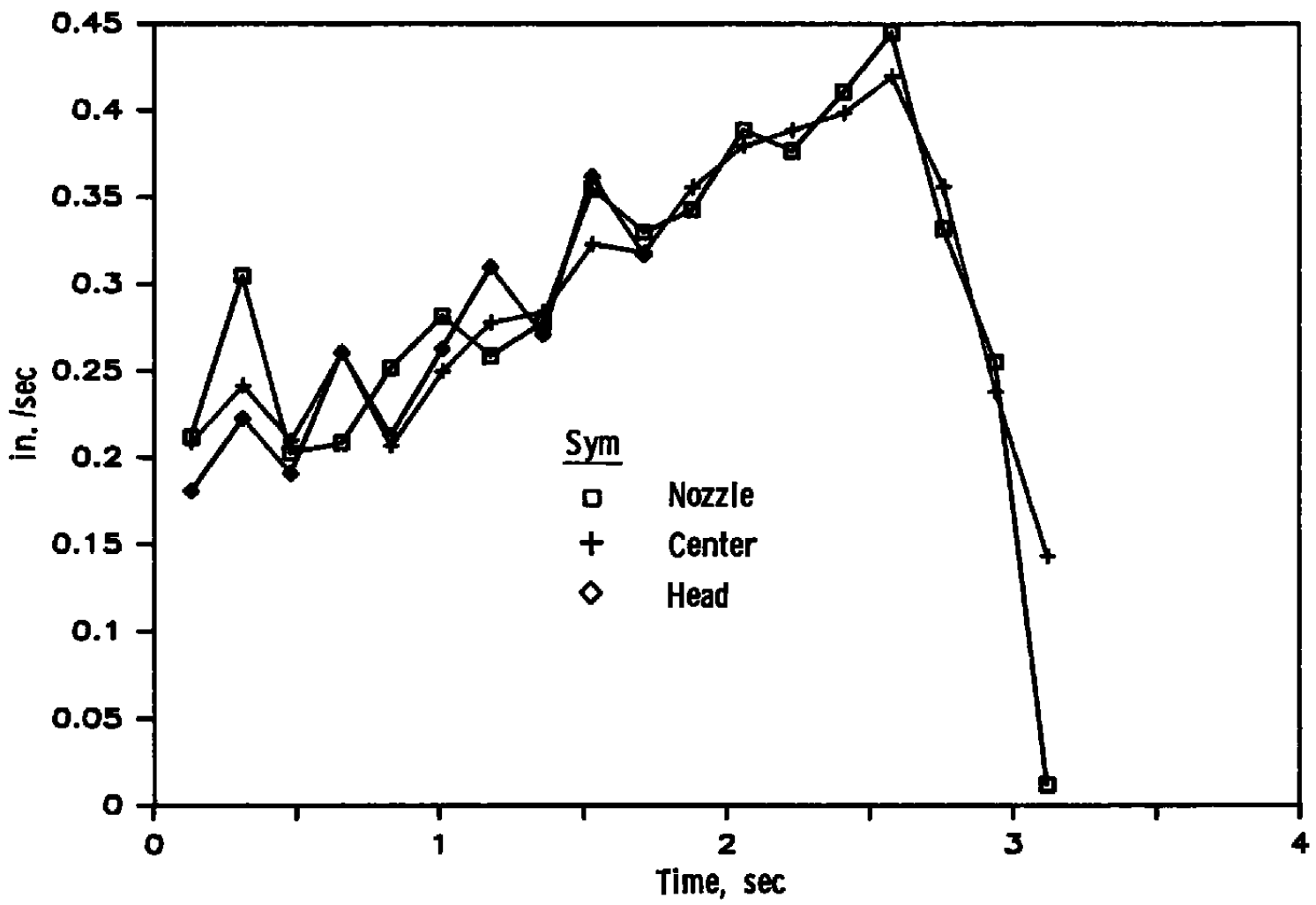


Figure 14. Burn-rate measurement, Motor No. 5.

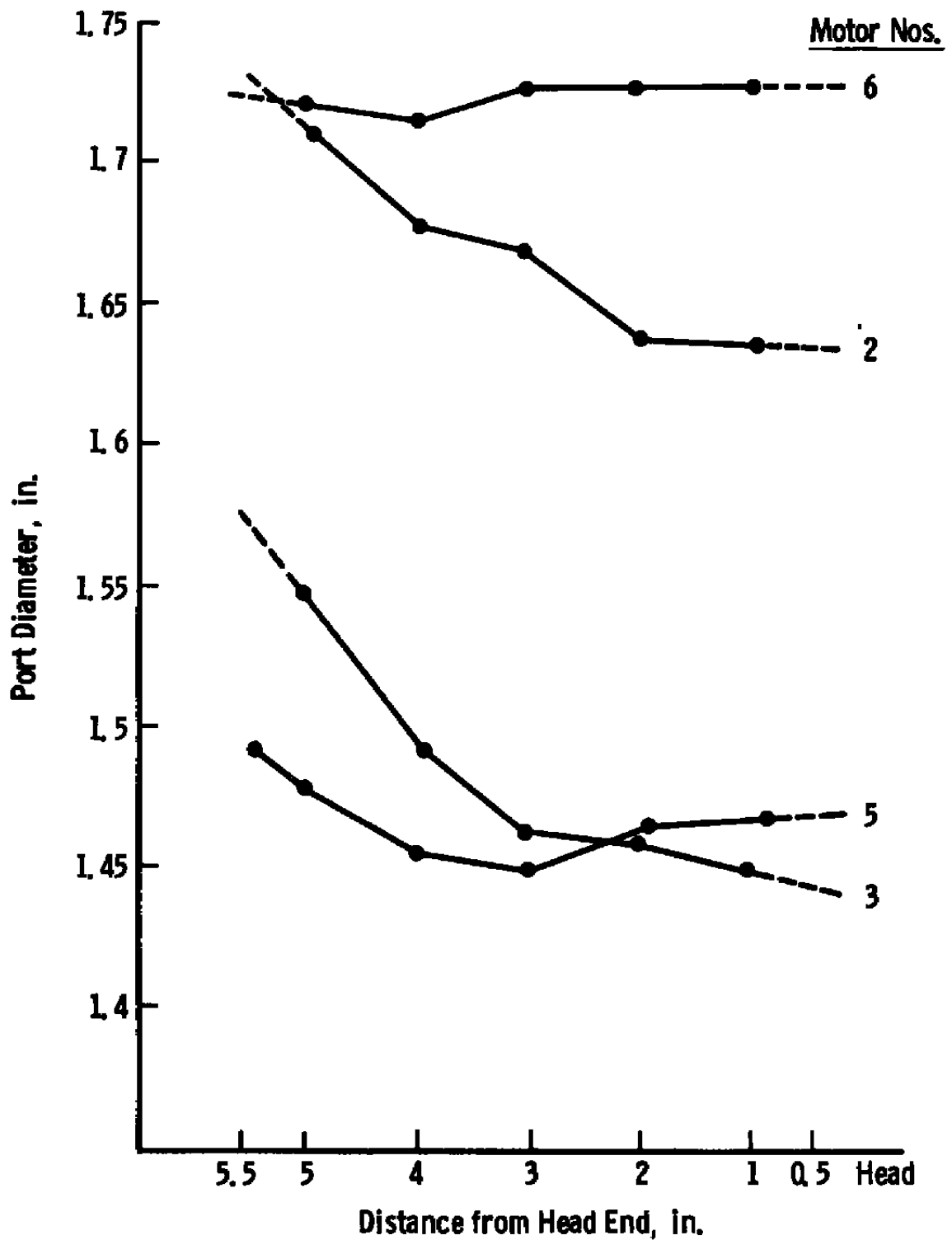


Figure 15. Port diameters at time two-thirds through burn.

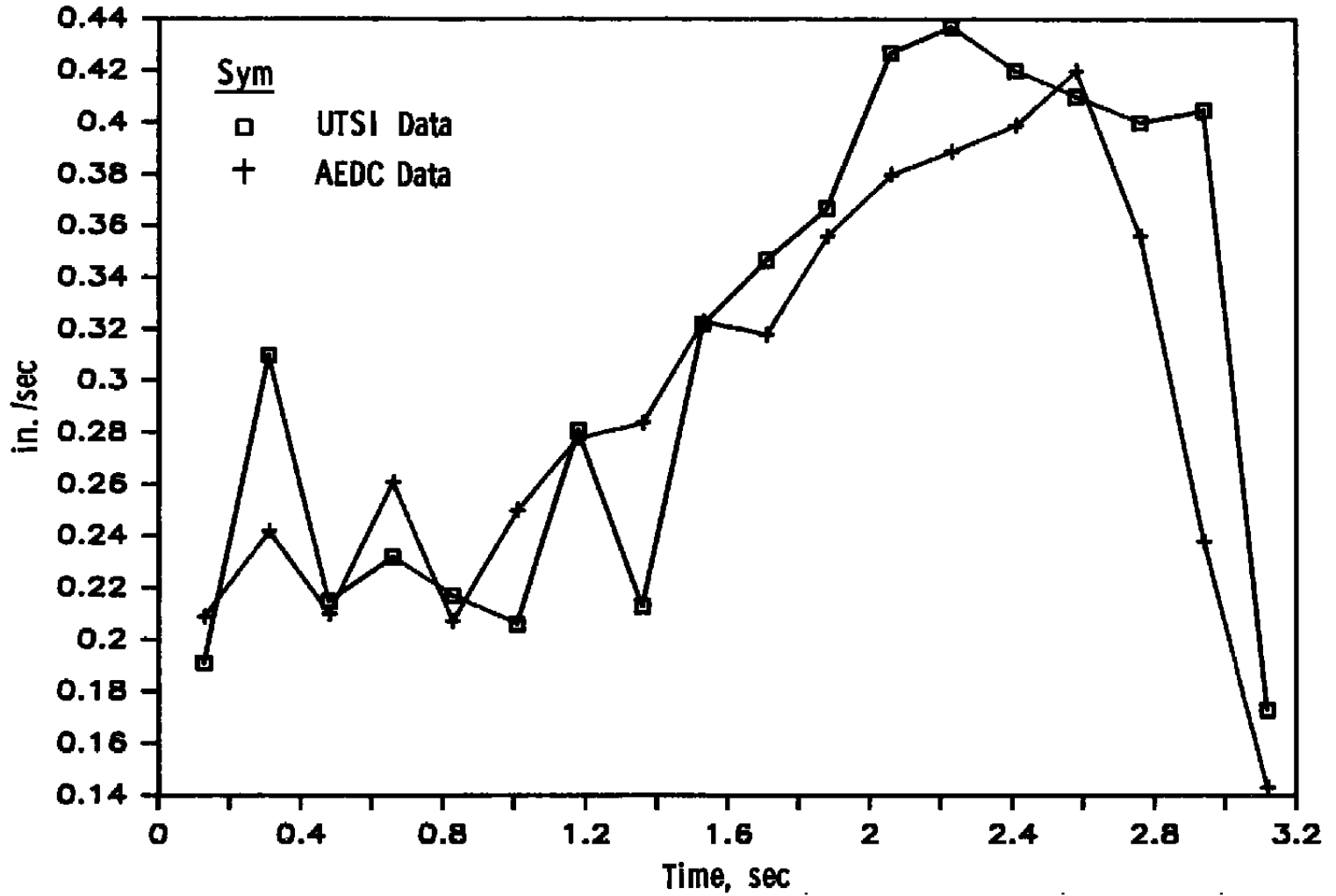


Figure 16. Comparison of UTSI and AEDC burn rates at the center of Motor 5.

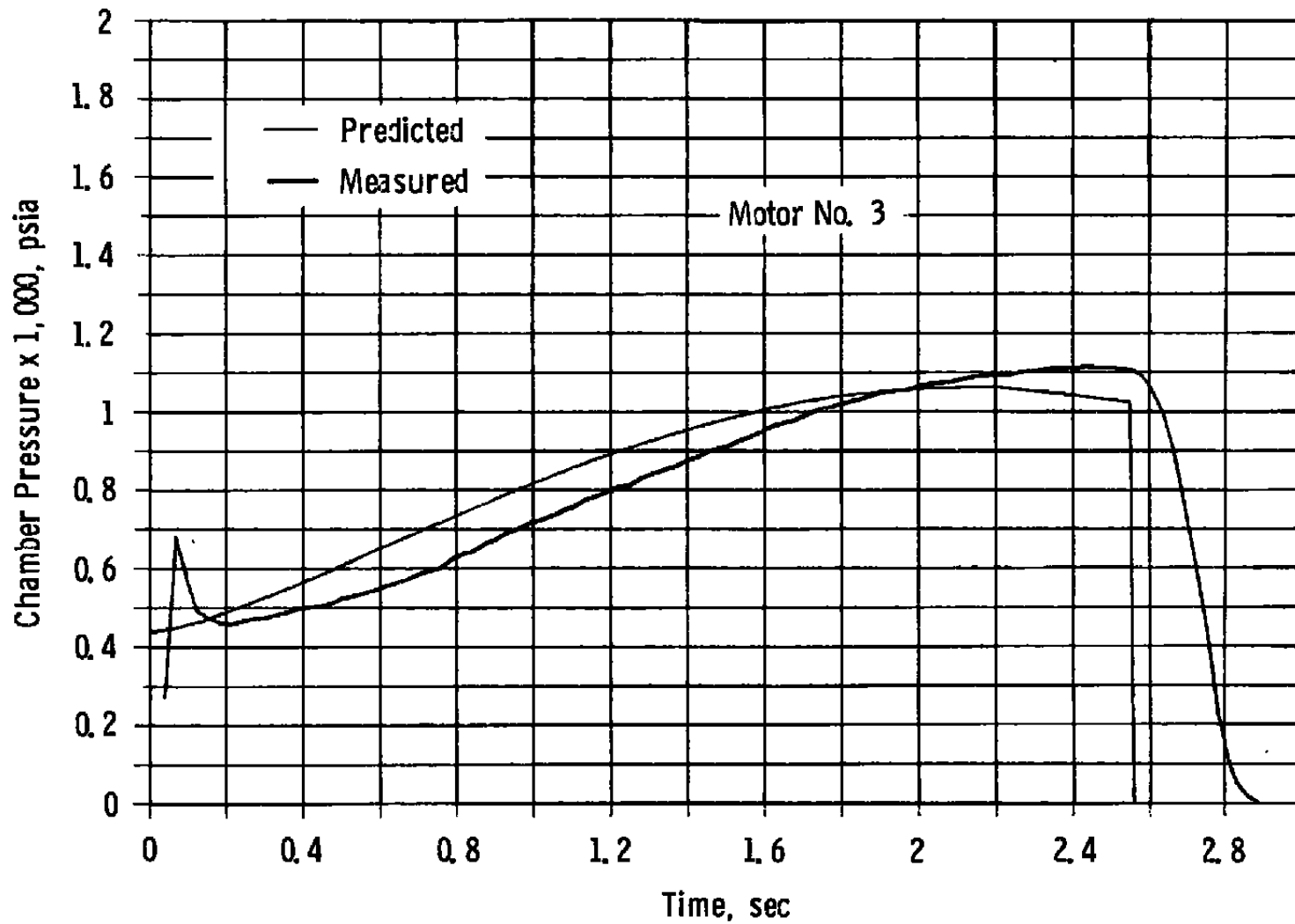


Figure 17. Predicted and measured pressures for high erosive motor.

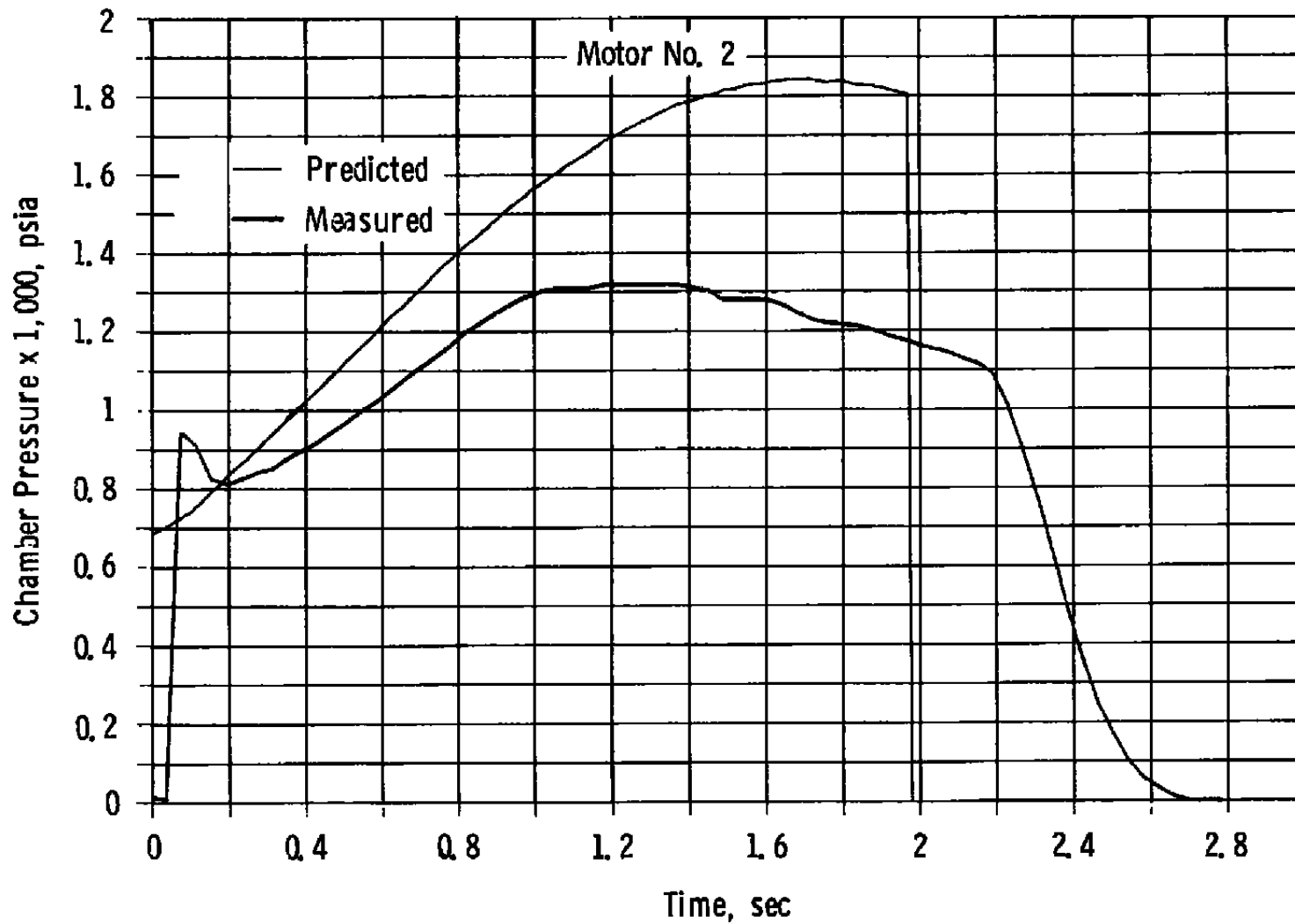


Figure 18. Predicted and measured pressures for mild erosive motor.

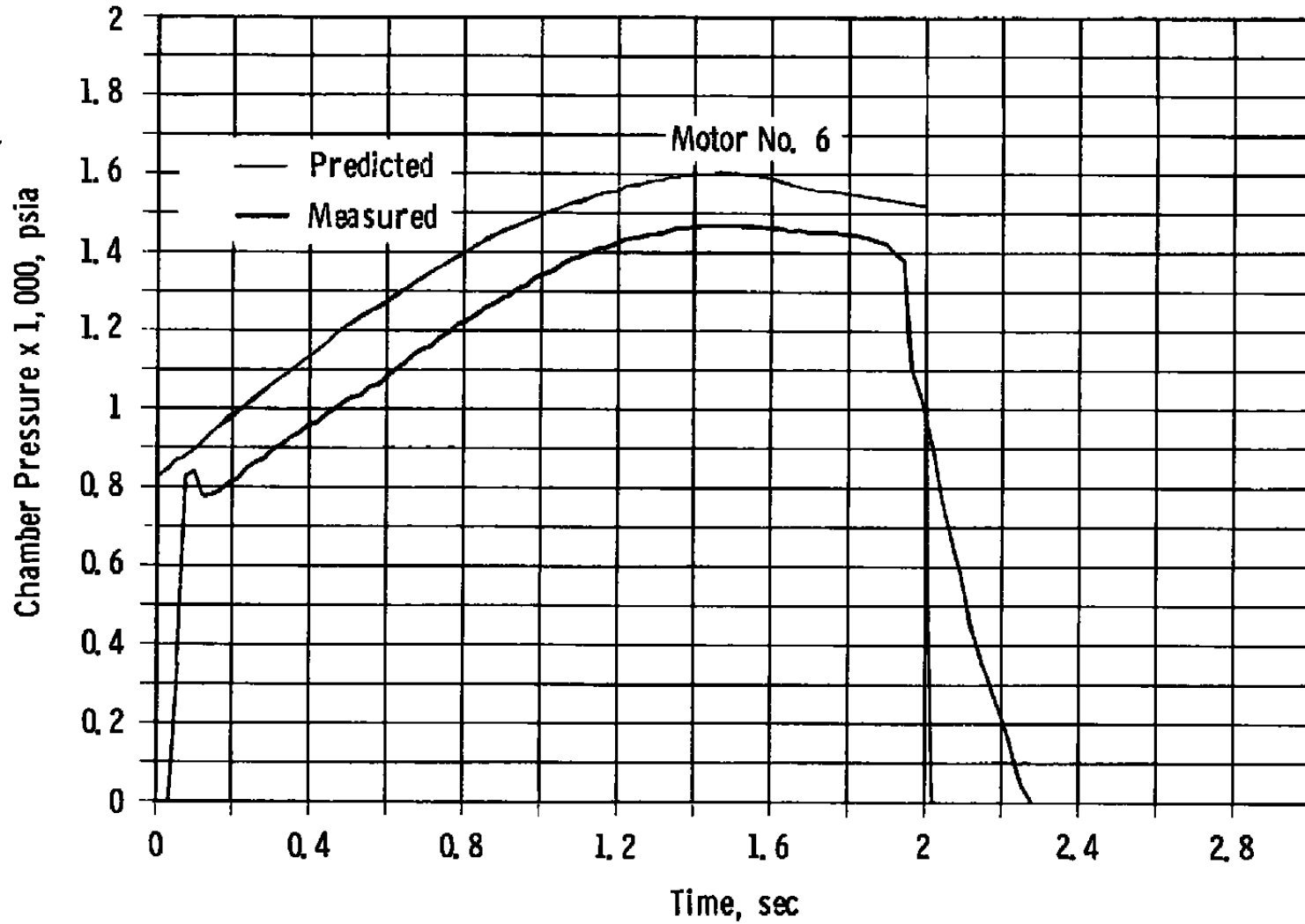


Figure 19. Predicted and measured pressures for nonerosive motor.

**Table 1. Propellant Formulation**

Ingredient	Weight, percent
Graphite	0.5
ZrC	1.9
AP	85.6
Binder	12.9

**Table 2. Motor Geometry Parameters Affecting Erosive Burning Severity**

Burning Category	Propellant Bore Diameter, in.	Nozzle Throat Diameter, in.
Nonerosive	0.625	0.303
Mild Erosive	0.340	0.278
High Erosive	0.340	0.323

**Table 3. Specifications of Cineradiography System**

<b>Flash X-Ray System HP 2722</b>
a. Power: 180 kv at 3,600 amp
b. Pulse Rate: $10^{-1}$ (Hipotronics Power Supply)
c. Pulse Width: 25 nsec
d. Effective Aperture: 1.8 mm
e. Penetration: 1.0-in. Aluminum at 1 m
<b>Film Changer (Schonander AOT 24-30)</b>
a. Film Size: 10 by 12 in.
b. Screens: 3M <sup>®</sup> Trimax 12
c. Recording Rate: 6 frames per sec, max
d. Max No. of Exposures: 30
e. Film I. D.: Date, Exposure No., Test No.
<b>Film</b>
a. 3M <sup>®</sup> XUD
b. Resolution (Includes Screens): 4 mil

**Table 4. Ballistic Performance Summary**

General Information						
Test Nos. (Motor Nos.)	1	2	3	4	5	6
Test Date	12/16/83	1/12/84	1/18/84	1/20/84	1/23/84	1/25/84
Grain S/N	-4	-2	-6	-3	-7	-8
Erosive Burn	None	Mild	High	Mild	High	None
Ambient Conditions						
Pressure, psia	14.32	14.27	14.21	14.38	14.27	14.04
Temp., °F	25	30	32	22	40	38
Expended Motor Weight, lbm	1.48	1.25	1.30	1.32	1.27	1.30
Nozzle Measurements						
Throat Area, in. <sup>2</sup>						
Prefire	0.072	0.062	0.083	0.050	0.082	0.072
Postfire	0.095	0.093	0.092	0.048	0.099	0.087
Change, percent	31.9	50.0	10.8	-4.0	20.7	20.8
Ballistic Performance						
Ignition Delay, msec	43	33	37	37	34	33
Action Time, sec	2.303	2.540	2.827	2.503	2.996	2.242
Maximum Thrust, lbf	174.9	158.1	154.5	169.9	177.9	182.2
Maximum Chamber						
Pressure, psia	1,369	1,334	1,127	1,661	1,227	1,474
Total Impulse, lbf-sec	267.7	274.0	282.7	281.5	284.9	283.2
Specific Impulse, lbf-sec/lbm	180.9	219.2	217.5	213.2	224.3	217.8

**Table 5. Port Diameters Measured by AEDC  
and UTSI on Motor No. 5**

Time, sec	AEDC Data, in.	UTSI Data, in.
0	0.308	---
0.13	0.361	0.349
0.31	0.449	0.462
0.48	0.522	0.537
0.66	0.614	0.618
0.83	0.686	0.694
1.01	0.774	0.766
1.18	0.871	0.865
1.36	0.970	0.939
1.53	1.083	1.052
1.71	1.195	1.173
1.88	1.320	1.303
2.06	1.453	1.452
2.23	1.589	1.605
2.41	1.730	1.753
2.58	1.877	---
2.76	2.002	2.034
2.94	2.088	2.181
3.12	2.138	2.242

**Table 6. Experimental Values of Base  
Burn Rate Constants**  
( $r_b = cp^n$ )

Motor	c	n
2	0.0044	0.653
3	0.0179	0.434
5	0.0393	0.316
6	0.0046	0.615